PHYSICAL REVIEW D **95,** 114021 (2017)

Transport coefficients of two-flavor quark matter from the Kubo formalism

Arus Harutyunyan[*] and Dirk H. Rischke[†]
Institute for Theoretical Physics, Goethe University, D-60438 Frankfurt am Main, Germany

Armen Sedrakian[‡]
Frankfurt Institute for Advanced Studies, D-60438 Frankfurt am Main, Germany
and Institute for Theoretical Physics, Goethe University, D-60438 Frankfurt am Main, Germany
(Received 17 February 2017; published 23 June 2017)

The transport coefficients of quark matter at nonzero chemical potential and temperature are computed within the two-flavor Nambu–Jona-Lasinio model. We apply the Kubo formalism to obtain the thermal (κ) and electrical (σ) conductivities as well as an update of the shear viscosity (η) by evaluating the corresponding equilibrium two-point correlation functions to leading order in the $1/N_c$ expansion. The Dirac structure of the self-energies and spectral functions is taken into account as these are evaluated from the meson-exchange Fock diagrams for on-mass-shell quarks. We find that the thermal and electrical conductivities are decreasing functions of temperature and density above the Mott temperature T_{M} of dissolution of mesons into quarks, the main contributions being generated by the temporal and vector components of the spectral functions. The coefficients show a universal dependence on the ratio T/T_{M} for different densities, i.e., the results differ by a chemical-potential dependent constant. We also show that the Wiedemann-Franz law for the ratio σ/κ does not hold. The ratio η/s, where s is the entropy density, is of order of unity (or larger) close to the Mott temperature and, as the temperature increases, approaches the AdS/CFT bound $1/4\pi$. It is also conjectured that the ratio $\kappa T/c_V$, with c_V being the specific heat, is bounded from below by $1/18$.

DOI: 10.1103/PhysRevD.95.114021

I. INTRODUCTION

The transport coefficients of strongly interacting matter in the regime where quarks are liberated to form an interacting quark-gluon plasma are of interest in a number of contexts. The high-temperature and low-density regime of the phase diagram of deconfined QCD matter is explored by heavy-ion collision experiments at RHIC and LHC, the collective dynamics of which is well described by hydrodynamical models with an extremely low value of the shear viscosity [1–9]. The high-density and low-temperature regime of the phase diagram is of great interest in the astrophysics of compact stars, where transport coefficients of deconfined QCD matter are an important input in modelling an array of astrophysical phenomena [10–13]. The intermediate regime of moderately dense and cold deconfined QCD matter, which is targeted by the FAIR program at GSI [14] and the NICA facility at JINR [15], provides a further motivation for studies of the transport coefficients in moderately dense QCD matter close to the chiral phase-transition line.

The nonperturbative nature of QCD in the phenomenologically interesting regimes mentioned above precludes the computation of the transport coefficients in full QCD, therefore effective models that capture its low-energy dynamics are required. In this work we use the Nambu–Jona-Lasinio (NJL) model [16,17], which provides a well-tested framework of low-energy QCD for studies of vacuum and in-matter properties of ensembles of quarks [18–20]. Because it captures the dynamical chiral symmetry-breaking feature of QCD it is most suited for the studies of transport coefficients in the vicinity of the chiral phase transition, where the elementary processes contributing to the scattering-matrix elements are dominated by mesonic fluctuations.

The transport formalism based on the Boltzmann equation for the quark distribution functions can be applied to strongly interacting ensembles in the limit where the quasiparticle concept is applicable; in that case the collision integral is dominated by two-body collisions between quarks moving in a mean-field between collisions. In this work we use the Kubo-Zubarev formalism [21,22] as an alternative, in which the transport coefficients are computed from equilibrium correlation functions at nonzero temperature and density. It provides a general framework valid for a strongly interacting system, which is characterized by nontrivial spectral functions, but requires a resummation of an infinite series of diagrams in order to obtain the correct scaling of the transport coefficients with the coupling (even in the weak-interaction regime).

The understanding of the elliptic flow observed at heavy-ion collider experiments in terms of dissipative

[*]arus@th.physik.uni-frankfurt.de
[†]drischke@th.physik.uni-frankfurt.de
[‡]sedrakian@fias.uni-frankfurt.de

hydrodynamics, in particular the description of the elliptic flow by a low shear viscosity-to-entropy density ratio of the deconfined quark phase stimulated extensive studies of the shear viscosity of strongly interacting matter. Transport coefficients of QCD matter have been investigated using various methods including perturbative QCD [23–30], equilibrium correlation functions within the Kubo formalism [31–38], transport simulations of the Boltzmann equation [39–42], relaxation-time approximation to the Boltzmann equation [43–46], lattice methods [47–52] and holographic methods [53–58] with the main emphasis on the low values of the shear viscosity-to-entropy density ratio indicated by the hydrodynamical modeling of heavy-ion collision experiments [1–9]. The shear viscosity of quark matter was computed within the NJL model using the Kubo formalism by several authors [32–37]. The problem of the resummation of an infinite series of loops required to obtain the finite-temperature correlation functions of quark matter is simplified by applying a $1/N_c$ power-counting scheme [59], where N_c is the number of colors. At leading order the resummation then reduces to keeping a single-loop diagram with full (dressed) propagators. Close to the chiral phase transition the quark self-energies are dominated by processes involving mesonic fluctuations, which can be obtained within the NJL model consistent with the two-point correlation functions.

In this work we compute the transport coefficients of quark matter at nonzero temperature and density within the NJL model and the Kubo-Zubarev formalism. Our main results concern the electrical and thermal conductivities of quark matter within the setup appropriate for relativistic quantum fields [60,61]. These would enter the hydrodynamical description of a dense quark-gluon plasma in the cases where thermal and charge relaxations play a phenomenological role. We discuss and update for completeness the shear viscosity of quark matter which was already studied in Refs. [32–35]. We consider the regime where the quark self-energies are dominated by mesonic fluctuations, i.e., the regime close to the chiral phase-transition line, which is relevant for heavy-ion collisions. Although our method and results can be straightforwardly applied to the dense and cold regime of compact stars, a number of factors, such as nonzero isospin, color superconductivity, and the presence of leptons, would require additional effort.

The paper is organized as follows. Section II derives the expressions for the thermal and electrical conductivities from the Kubo-Zubarev formalism. In Sec. III we discuss the quark and meson masses within the two-flavor NJL model and derive the spectral function of quarks taking into account the Dirac structure of the self-energies. Numerical results for the transport coefficients are given in Sec. IV. Our results are summarized in Sec. V. Appendix A is devoted to the equilibrium properties of the two-flavor NJL model, Appendix B computes the quark self-energy due to meson exchange, and finally Appendix C lists some of the relevant thermodynamic relations used in our computations. We use natural (Gaussian) units with $\hbar = c = k_B = k_e = 1$, $e = \sqrt{4\pi\alpha}$, $\alpha = 1/137$, and the metric signature $(+,-,-,-)$.

II. KUBO FORMULAS FOR TRANSPORT COEFFICIENTS

The Kubo-Zubarev formalism relates the transport properties of a statistical ensemble to different types of *equilibrium* correlation functions, which in turn can be computed using equilibrium many-body techniques [21,22]. We start our discussion with the Lagrangian of the underlying effective model, as it will specify the power counting required for the computation of the two-point correlation functions.

A. Lagrangian

We consider two-flavor quark matter described by the NJL Lagrangian of the form

$$\mathcal{L} = \bar{\psi}(i\partial\!\!\!/ - m_0)\psi + \frac{G}{2}[(\bar{\psi}\psi)^2 + (\bar{\psi} i\gamma_5 \boldsymbol{\tau}\psi)^2], \quad (1)$$

where $\psi = (u, d)^T$ is the isodoublet quark field, $m_0 = 5.5$ MeV is the current quark mass, $G = 10.1\ \mathrm{GeV}^{-2}$ is the effective four-fermion coupling constant, and $\boldsymbol{\tau}$ is the vector of Pauli isospin matrices. This Lagrangian describes four-fermion scalar-isoscalar and pseudoscalar-isovector interactions between quarks with the corresponding bare vertices $\Gamma_s^0 = 1$ and $\Gamma_{ps}^0 = i\boldsymbol{\tau}\gamma_5$. The symmetrized energy-momentum tensor is given in the standard fashion by

$$T_{\mu\nu} = \frac{i}{2}(\bar{\psi}\gamma_\mu\partial_\nu\psi + \bar{\psi}\gamma_\nu\partial_\mu\psi) - g_{\mu\nu}\mathcal{L}, \quad (2)$$

and the quark-number and charge currents are defined as

$$N_\mu = \bar{\psi}\gamma_\mu\psi, \qquad J_\mu = \bar{\psi}\,\hat{Q}\,\gamma_\mu\psi, \quad (3)$$

where

$$\hat{Q} = e\begin{pmatrix} 2/3 & 0 \\ 0 & -1/3 \end{pmatrix} \quad (4)$$

is the charge matrix in flavor space, with e being the elementary charge. The expression for the energy-momentum tensor (2) is symmetric in its indices; this form is necessary for the implementation in the Kubo formulas.

B. Thermal and electrical conductivities

Within the Kubo-Zubarev approach the thermal and electrical conductivities are given by

$$\kappa = -\frac{\beta}{3}\frac{d}{d\omega}\mathrm{Im}\Pi_\kappa^R(\omega)|_{\omega=0}, \quad (5)$$

$$\sigma = -\frac{1}{3}\frac{d}{d\omega}\mathrm{Im}\Pi^R_\sigma(\omega)|_{\omega=0}, \tag{6}$$

where $\beta = T^{-1}$ is the inverse temperature, and the retarded correlation functions on the right-hand sides are defined as [22,61]

$$\Pi^R_\kappa(\omega) = i\int_0^\infty dt e^{i\omega t}\int d\boldsymbol{r}\langle[q_\mu(\boldsymbol{r},t), q^\mu(0)]\rangle_0, \tag{7}$$

$$\Pi^R_\sigma(\omega) = i\int_0^\infty dt e^{i\omega t}\int d\boldsymbol{r}\langle[j_\mu(\boldsymbol{r},t), j^\mu(0)]\rangle_0, \tag{8}$$

i.e., they are the statistical averages of commutators (denoted by $[\cdot,\cdot]$) of the heat and electrical currents defined, respectively, as

$$q_\mu = \Delta_{\mu\alpha}u_\beta T^{\alpha\beta} - h\Delta_{\mu\alpha}N^\alpha, \tag{9}$$

$$j_\mu = \Delta_{\mu\alpha}J^\alpha. \tag{10}$$

Here u_β is the 4-velocity of the fluid, $\Delta_{\mu\nu} = g_{\mu\nu} - u_\mu u_\nu$ is the projector on the direction transverse to the fluid velocity, h is the enthalpy per particle, and the energy-momentum tensor $T^{\mu\nu}$ is assumed to be symmetric in its indices. Note that the heat current (9) differs from the net energy flow by the particle-convection term $\propto h$.

Equations (5)–(8) apply to arbitrary quantum statistical ensembles without restrictions on the strength of the couplings of the underlying theory. In the following we will derive more specific expressions suitable for the NJL model with contact scalar and pseudo-scalar couplings among quarks by applying the $1/N_c$ expansion to select the dominant diagrams contributing to the correlation functions.

It is convenient to evaluate the correlation functions of interest using the thermal equilibrium Green's functions of the imaginary-time Matsubara technique. In the fluid rest frame $u_\mu = (1,0,0,0)$, $\Delta_{\mu\nu} = \mathrm{diag}(0,-1,-1,-1)$, and the Matsubara correlation functions read

$$\Pi^M_\kappa(\omega_n) = \Pi^M_{TT}(\omega_n) - 2h\Pi^M_{TN}(\omega_n) + h^2\Pi^M_{NN}(\omega_n), \tag{11}$$

$$-\frac{1}{3}\Pi^M_{TT}(\omega_n) = \int_0^\beta d\tau e^{i\omega_n\tau}\int d\boldsymbol{r}\langle T_\tau(T_{01}(\boldsymbol{r},\tau), T_{01}(0))\rangle_0, \tag{12}$$

$$-\frac{1}{3}\Pi^M_{TN}(\omega_n) = \int_0^\beta d\tau e^{i\omega_n\tau}\int d\boldsymbol{r}\langle T_\tau(T_{01}(\boldsymbol{r},\tau), N_1(0))\rangle_0, \tag{13}$$

$$-\frac{1}{3}\Pi^M_{NN}(\omega_n) = \int_0^\beta d\tau e^{i\omega_n\tau}\int d\boldsymbol{r}\langle T_\tau(N_1(\boldsymbol{r},\tau), N_1(0))\rangle_0, \tag{14}$$

$$-\frac{1}{3}\Pi^M_\sigma(\omega_n) = \int_0^\beta d\tau e^{i\omega_n\tau}\int d\boldsymbol{r}\langle T_\tau(J_1(\boldsymbol{r},\tau), J_1(0))\rangle_0, \tag{15}$$

where $T_{01}(\boldsymbol{r},\tau)$, $N_1(\boldsymbol{r},\tau)$, and $J_1(\boldsymbol{r},\tau)$ are obtained from $T_{01}(\boldsymbol{r},t)$, $N_1(\boldsymbol{r},t)$, and $J_1(\boldsymbol{r},t)$ via Wick rotation $t \to -i\tau$, T_τ is the time-ordering operator for imaginary time τ, and the factor 3 arises from summation over the directions of isotropic three-dimensional space. In Eq. (11) we decomposed the thermal current according to Eq. (9) and used the symmetry of the correlation function with respect to its arguments [61]. The required retarded correlation functions (7) and (8) can be obtained from (11)–(15) by analytic continuation $i\omega_n \to \omega + i\delta$. Note that the transformation to imaginary time implies a change of the derivative $\partial_0 \to i\partial_\tau$. Because $T_{\mu\nu}$, and therefore also N_μ and J_μ, are bosonic operators, the Matsubara frequencies assume even integer values $\omega_n = 2\pi nT$, $n = 0, \pm 1, \ldots$. The T_{01} component of Eq. (2) is given by

$$T_{01}(\boldsymbol{r},\tau) = i\bar\psi(\boldsymbol{r},\tau)\frac{\gamma_0}{2}\partial_1\psi(\boldsymbol{r},\tau) + i\bar\psi(\boldsymbol{r},\tau)\frac{\gamma_1}{2}i\partial_\tau\psi(\boldsymbol{r},\tau).$$

Substituting $T_{01}(\boldsymbol{r},\tau)$, $N_1(\boldsymbol{r},\tau)$, and $J_1(\boldsymbol{r},\tau)$ into Eqs. (11)–(15) we obtain

$$-\frac{1}{3}\Pi^M_{TT}(\omega_n) = \sum_{\alpha,\alpha'}\int_0^\beta d\tau e^{i\omega_n\tau} \times \int d\boldsymbol{r}\left\langle T_\tau\left(i\bar\psi\frac{\gamma_\mu}{2}\partial_\alpha\psi|_{(\boldsymbol{r},\tau)}, i\bar\psi\frac{\gamma_{\mu'}}{2}\partial_{\alpha'}\psi|_0\right)\right\rangle_0, \tag{16}$$

$$-\frac{1}{3}\Pi^M_{TN}(\omega_n) = \sum_{\alpha}\int_0^\beta d\tau e^{i\omega_n\tau} \times \int d\boldsymbol{r}\left\langle T_\tau\left(i\bar\psi\frac{\gamma_\mu}{2}\partial_\alpha\psi|_{(\boldsymbol{r},\tau)}, \bar\psi\gamma_1\psi|_0\right)\right\rangle_0, \tag{17}$$

$$-\frac{1}{3}\Pi^M_{NN}(\omega_n) = \int_0^\beta d\tau e^{i\omega_n\tau}\int d\boldsymbol{r}\langle T_\tau(\bar\psi\gamma_1\psi|_{(\boldsymbol{r},\tau)}, \bar\psi\gamma_1\psi|_0)\rangle_0, \tag{18}$$

$$-\frac{1}{3}\Pi^M_\sigma(\omega_n) = \int_0^\beta d\tau e^{i\omega_n\tau} \times \int d\boldsymbol{r}\langle T_\tau(\bar\psi\,\hat Q\gamma_1\psi|_{(\boldsymbol{r},\tau)}, \bar\psi\,\hat Q\gamma_1\psi|_0)\rangle_0, \tag{19}$$

where $\alpha, \alpha', \mu, \mu'$ assume values 1,0, with $\mu \neq \alpha, \mu' \neq \alpha'$, i.e., the sums in Eqs. (16) and (17) contain four and two terms, respectively.

To select the relevant diagrams contributing to the correlation functions we apply the $1/N_c$ power-counting

scheme, in which each loop contributes a factor of N_c from the trace over color space [32–37,59]. Each coupling G (which is associated with a pair of $\Gamma^0_{s/ps}$ matrices) contributes a factor of $1/N_c$. Therefore, for any given number of $\Gamma^0_{s/ps}$ vertices the leading diagram in the $1/N_c$ approximation is the one that has the maximum number of loops. Figure 1 shows the diagrammatic expansion for the two-point correlation function, which we define in a generic form

$$\Pi^{\alpha\alpha'}_{\mu\mu'}(\omega_n) = \int_0^\beta d\tau e^{i\omega_n\tau} \times \int d\boldsymbol{r}\langle T_\tau(i\bar{\psi}\gamma_\mu\partial^\alpha\psi|_{(\boldsymbol{r},\tau)}, i\bar{\psi}\gamma_{\mu'}\partial^{\alpha'}\psi|_0)\rangle_0, \quad (20)$$

where $\partial_\alpha = (i\partial_\tau, \partial_i)$. The diagrams are arranged according to the $1/N_c$ expansion. The first line contains a loop and no coupling G and is of order N_c; the second line contains two loops and a coupling, and therefore is again of order of N_c; the third line, which contains a loop and a coupling, is of order of N_c^0. Thus, the correlation function (20) in the leading $[\mathcal{O}(N_c^1)]$ order is given by a sum of loop diagrams which contain the single-loop contribution (first line in Fig. 1)

$$T\sum_l \int \frac{d\boldsymbol{p}}{(2\pi)^3} p^\alpha p^{\alpha'} \mathrm{Tr}[\gamma_\mu G(\boldsymbol{p}, i\omega_l + i\omega_n)\gamma_{\mu'} G(\boldsymbol{p}, i\omega_l)], \quad (21)$$

plus multiloop contributions which necessarily contain loop contributions of the type

$$T\sum_l \int \frac{d\boldsymbol{p}}{(2\pi)^3} p^\alpha \mathrm{Tr}[\gamma_\mu G(\boldsymbol{p}, i\omega_l + i\omega_n)\Gamma^0_{s/ps} G(\boldsymbol{p}, i\omega_l)], \quad (22)$$

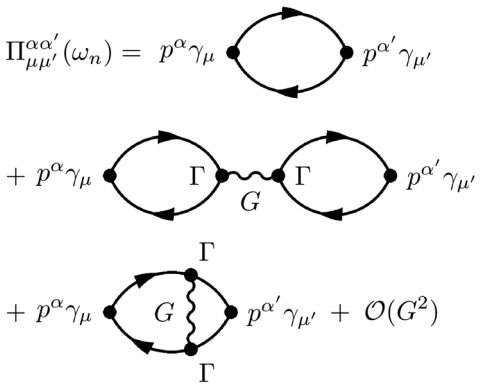

FIG. 1. Contributions to the two-point correlation functions from $\mathcal{O}(N_c^1)$ (first and second lines) and $\mathcal{O}(N_c^0)$ (the third line) diagrams which contain a single interaction line G.

see the second line in Fig. 1. Here $G(\boldsymbol{p}, i\omega_l)$ is the dressed Matsubara Green's function of quarks, the summation goes over fermionic Matsubara frequencies $\omega_l = \pi(2l+1)T - i\mu$, $l = 0, \pm1, \ldots$, with temperature T and chemical potential μ; (in isospin-symmetric two-flavor quark matter there is a single chemical potential for both u and d quarks). The traces should be taken in Dirac, color, and flavor space. The Lorentz structure of the Green's function implies that (a) diagrams of type (22) with pseudoscalar vertices vanish due to the trace over the Dirac space and (b) those with scalar vertices vanish if $\alpha \neq \mu$, because the integrand has an odd power of momentum, which implies that the momentum integral vanishes in isotropic momentum space. Thus, the only term contributing to Eq. (16) is the one-loop expression (21). In the same way one can see that the multiloop diagrams vanish also for the other three correlation functions (17)–(19). Thus, for the correlation functions (16)–(19) we obtain

$$\frac{1}{3}\Pi^M_{TT}(\omega_n) = \frac{T}{4}\sum_l \sum_{\alpha,\alpha'} \int \frac{d\boldsymbol{p}}{(2\pi)^3} p_\alpha p_{\alpha'} \times \mathrm{Tr}[\gamma_\mu G(\boldsymbol{p}, i\omega_l + i\omega_n)\gamma_{\mu'} G(\boldsymbol{p}, i\omega_l)], \quad (23)$$

$$\frac{1}{3}\Pi^M_{TN}(\omega_n) = \frac{T}{2}\sum_l \sum_{\alpha} \int \frac{d\boldsymbol{p}}{(2\pi)^3} p_\alpha \times \mathrm{Tr}[\gamma_1 G(\boldsymbol{p}, i\omega_l + i\omega_n)\gamma_\mu G(\boldsymbol{p}, i\omega_l)], \quad (24)$$

$$\frac{1}{3}\Pi^M_{NN}(\omega_n) = T\sum_l \int \frac{d\boldsymbol{p}}{(2\pi)^3} \times \mathrm{Tr}[\gamma_1 G(\boldsymbol{p}, i\omega_l + i\omega_n)\gamma_1 G(\boldsymbol{p}, i\omega_l)], \quad (25)$$

$$\frac{1}{3}\Pi^M_{\sigma}(\omega_n) = T\sum_l \int \frac{d\boldsymbol{p}}{(2\pi)^3} \times \mathrm{Tr}[\hat{Q}\gamma_1 G(\boldsymbol{p}, i\omega_l + i\omega_n)\hat{Q}\gamma_1 G(\boldsymbol{p}, i\omega_l)], \quad (26)$$

where $p_\alpha, p_{\alpha'}$ assume values p_1 and $p_0 = i\omega_l + i\omega_n/2$. Note that the expressions (23)–(26) are valid in a wider context, i.e., in any relativistic theory (both bosonic and fermionic) where the single-loop (skeleton) diagram with fully dressed propagators constitutes the leading-order contribution in the power-counting scheme.

The Matsubara summations appearing in these expressions can be cast into the general form

$$S_{\mu\nu}[f](\boldsymbol{p}, i\omega_n) = T\sum_l \mathrm{Tr}[\gamma_\mu G(\boldsymbol{p}, i\omega_l + i\omega_n) \times \gamma_\nu G(\boldsymbol{p}, i\omega_l)] f(i\omega_l + i\omega_n/2), \quad (27)$$

where $f(z) = z^n$ with $n = 0, 1, 2$. The summation is standard upon introducing the spectral representation of the temperature Green's functions

$$G(\boldsymbol{p},z)=\int_{-\infty}^{\infty}d\varepsilon\frac{A(\boldsymbol{p},\varepsilon)}{z-\varepsilon}, \tag{28}$$

where the spectral function is given by

$$A(\boldsymbol{p},\varepsilon)=-\frac{1}{2\pi i}[G^R(\boldsymbol{p},\varepsilon)-G^A(\boldsymbol{p},\varepsilon)], \tag{29}$$

and $G^{R/A}$ are the retarded/advanced Green's functions. After summation and subsequent analytical continuation $i\omega_n\to\omega+i\delta$ we find

$$S_{\mu\nu}[f](\boldsymbol{p},\omega)=\int_{-\infty}^{\infty}d\varepsilon\int_{-\infty}^{\infty}d\varepsilon'\mathrm{Tr}[\gamma_\mu A(\boldsymbol{p},\varepsilon')\gamma_\nu A(\boldsymbol{p},\varepsilon)]\times\frac{\tilde{n}(\varepsilon)f(\varepsilon+\omega/2)-\tilde{n}(\varepsilon')f(\varepsilon'-\omega/2)}{\varepsilon-\varepsilon'+\omega+i\delta}, \tag{30}$$

where $n(\varepsilon)=[e^{\beta(\varepsilon-\mu)}+1]^{-1}$ is the Fermi distribution function and $\tilde{n}(\varepsilon)=n(\varepsilon)-1/2$. Substituting this result into the correlation functions (23)-(26) we obtain compact expressions in terms of Eq. (30)

$$\frac{1}{3}\Pi_{TT}(\omega)=\frac{1}{4}\int\frac{d\boldsymbol{p}}{(2\pi)^3}\{p_1^2S_{00}[f=1]+2p_1S_{01}[f=\varepsilon]+S_{11}[f=\varepsilon^2]\}(\boldsymbol{p},\omega), \tag{31}$$

$$\frac{1}{3}\Pi_{TN}(\omega)=\frac{1}{2}\int\frac{d\boldsymbol{p}}{(2\pi)^3}\{p_1S_{10}[f=1]+S_{11}[f=\varepsilon]\}(\boldsymbol{p},\omega), \tag{32}$$

$$\frac{1}{3}\Pi_{NN}(\omega)=\int\frac{d\boldsymbol{p}}{(2\pi)^3}S_{11}[f=1](\boldsymbol{p},\omega), \tag{33}$$

$$\frac{1}{3}\Pi_{\sigma}(\omega)=\frac{1}{3}\Pi_{NN}(\omega)\times\frac{\mathrm{Tr}\hat{Q}^2}{N_f}, \tag{34}$$

with N_f being the number of flavors. These expressions can now be substituted into Eqs. (5) and (6) to find the thermal and electrical conductivities. It is, however, convenient to first separate the real and imaginary parts in Eq. (30) via the Dirac identity in order to find the required $\omega\to 0$ limit. We find from Eq. (30)

$$\frac{d}{d\omega}\mathrm{Im}S_{\mu\nu}[f](\boldsymbol{p},\omega)|_{\omega=0}=\pi\int_{-\infty}^{\infty}d\varepsilon\frac{\partial n(\varepsilon)}{\partial\varepsilon}f(\varepsilon)\mathcal{T}_{\mu\nu}(\boldsymbol{p},\varepsilon), \tag{35}$$

where

$$\mathcal{T}_{\mu\nu}(\boldsymbol{p},\varepsilon)\equiv\mathrm{Tr}[\gamma_\mu A(\boldsymbol{p},\varepsilon)\gamma_\nu A(\boldsymbol{p},\varepsilon)]. \tag{36}$$

Using expressions (31)–(36) we finally obtain from Eqs. (5) and (6)

$$\kappa=-\frac{\pi}{4T}\int_{-\infty}^{\infty}d\varepsilon\frac{\partial n(\varepsilon)}{\partial\varepsilon}\int\frac{d\boldsymbol{p}}{(2\pi)^3}[p_1^2\mathcal{T}_{00}(\boldsymbol{p},\varepsilon)+2p_1(\varepsilon-2h)\mathcal{T}_{01}(\boldsymbol{p},\varepsilon)+(\varepsilon-2h)^2\mathcal{T}_{11}(\boldsymbol{p},\varepsilon)], \tag{37}$$

$$\sigma=-\pi\mathrm{Tr}\frac{\mathrm{Tr}\hat{Q}^2}{N_f}\int_{-\infty}^{\infty}d\varepsilon\frac{\partial n(\varepsilon)}{\partial\varepsilon}\int\frac{d\boldsymbol{p}}{(2\pi)^3}\mathcal{T}_{11}(\boldsymbol{p},\varepsilon). \tag{38}$$

Thus, the problem of computing the transport coefficients reduces to the determination of the spectral function of the quarks followed by computing the components of the trace $\mathcal{T}_{\mu\nu}(\boldsymbol{p},\varepsilon)$.

The quark spectral function in an isotropic medium has a general decomposition in terms of Lorentz-invariant components,

$$A(\boldsymbol{p},p_0)=-\frac{1}{\pi}(mA_s+p_0\gamma_0A_0-\boldsymbol{p}\cdot\boldsymbol{\gamma}A_v), \tag{39}$$

where the coefficients A_s,A_0,A_v are expressed in terms of the analogous components of the self-energy in Appendix A. Substituting the decomposition (39) into Eqs. (37) and (38) we obtain

$$\kappa=-\frac{N_cN_f}{\pi T}\int_{-\infty}^{\infty}d\varepsilon\frac{\partial n(\varepsilon)}{\partial\varepsilon}\times\int\frac{d\boldsymbol{p}}{(2\pi)^3}\{p_1^2(A_s^2m^2+A_0^2\varepsilon^2+A_v^2\boldsymbol{p}^2)+4p_1^2\varepsilon(\varepsilon-2h)A_0A_v-(\varepsilon-2h)^2\times(A_s^2m^2-A_0^2\varepsilon^2+A_v^2\boldsymbol{p}^2-2A_v^2p_1^2)\}, \tag{40}$$

$$\sigma=-\frac{4N_c}{\pi}\mathrm{Tr}\hat{Q}^2\int_{-\infty}^{\infty}d\varepsilon\frac{\partial n(\varepsilon)}{\partial\varepsilon}\times\int\frac{d\boldsymbol{p}}{(2\pi)^3}(-A_s^2m^2+A_0^2\varepsilon^2-A_v^2\boldsymbol{p}^2+2A_v^2p_1^2), \tag{41}$$

where we summed over the quark flavor (N_f) and color (N_c) numbers. Finally we note that the Lorentz-invariant coefficients A_s,A_0,A_v of the decomposition of the spectral function depend only on $\boldsymbol{p}^2$ and ε (see Appendix A), therefore the angular integration can be done trivially by substituting $p_1^2\to\boldsymbol{p}^2/3\equiv p^2/3$, after which we finally obtain

$$\kappa=-\frac{N_cN_f}{6\pi^3T}\int_{-\infty}^{\infty}d\varepsilon\frac{\partial n}{\partial\varepsilon}\int_0^{\Lambda}dpp^2\{[A_s^2(p,\varepsilon)m^2-A_0^2(p,\varepsilon)\varepsilon^2+A_v^2(p,\varepsilon)p^2][p^2-3(\varepsilon-2h)^2]+2[A_0(p,\varepsilon)\varepsilon+A_v(p,\varepsilon)(\varepsilon-2h)]^2p^2\}, \tag{42}$$

$$\sigma=\frac{40N_c\alpha}{27\pi^2}\int_{-\infty}^{\infty}d\varepsilon\frac{\partial n}{\partial\varepsilon}\int_0^{\Lambda}dpp^2[3A_s^2(p,\varepsilon)m^2-3A_0^2(p,\varepsilon)\varepsilon^2+A_v^2(p,\varepsilon)p^2], \tag{43}$$

where $\Lambda = 650$ MeV is the ultraviolet cutoff of the NJL model. Given the Lorentz components of the spectral function we are in a position to compute the thermal and electrical conductivities of two-flavor quark matter using our final expressions (42) and (43).

C. Shear viscosity

Within the Kubo formalism the shear viscosity is given as [60]

$$\eta = -\frac{1}{10}\frac{d}{d\omega}\mathrm{Im}\Pi^R_\eta(\omega)|_{\omega=0}, \tag{44}$$

where the retarded correlation function has the form

$$\Pi^R_\eta(\omega) = -i\int_0^\infty dt e^{i\omega t}\int d\boldsymbol{r}\langle[\pi_{\mu\nu}(\boldsymbol{r},t),\pi^{\mu\nu}(0)]\rangle_0, \tag{45}$$

with $\pi_{\mu\nu}$ being the shear-viscosity tensor, defined as

$$\pi_{\mu\nu} = \Delta^{\alpha\beta}_{\mu\nu}T_{\alpha\beta}, \tag{46}$$

where

$$\Delta^{\alpha\beta}_{\mu\nu} = \frac{\Delta^\alpha_\mu\Delta^\beta_\nu + \Delta^\beta_\mu\Delta^\alpha_\nu}{2} - \frac{1}{3}\Delta_{\mu\nu}\Delta^{\alpha\beta}. \tag{47}$$

It is useful to note that $\Delta^{\alpha\beta}_{\mu\nu}g_{\alpha\beta} = 0$ by definition, therefore the component of the energy-momentum tensor (2) containing $g_{\mu\nu}$ does not contribute to Eq. (46).

In the fluid rest frame $\Delta^j_i = \delta_{ij}$, $\Delta^0_0 = \Delta^j_0 = 0$, where i, $j = 1, 2, 3$, and δ_{ij} is the Kronecker symbol. In this frame only the spatial components of Eq. (46), $\pi_{ij} = T_{ij} - \delta_{ij}T_{mm}/3$, are nonzero. Then, the two-point correlation function (45) takes the form

$$\Pi^R_\eta(\omega) = -2i\int_0^\infty dt e^{i\omega t}\int d\boldsymbol{r}\langle[T_{11},T_{11}] - [T_{11},T_{22}] + 3[T_{12},T_{12}]\rangle_0, \tag{48}$$

where we took into account the isotropy of the medium and for the sake of brevity omitted the arguments of the T_{ij} tensors. Note that the commutator $[T_{11},(T_{11}-T_{22})]$ is manifestly nonzero at the operator level, and a computation shows that its statistical average does not vanish in an isotropic medium and cannot be neglected. The Matsubara counterpart of this retarded two-point function is given by

$$\Pi^M_\eta(\omega_n) = -2\int_0^\beta d\tau e^{i\omega_n\tau}\int d\boldsymbol{r}\langle T_\tau(T_{11}(\boldsymbol{r},\tau)T_{11}(0) - T_{11}(\boldsymbol{r},\tau)T_{22}(0) + 3T_{12}(\boldsymbol{r},\tau)T_{12}(0))\rangle_0. \tag{49}$$

We next compute the components of the energy-momentum tensor contributing to Eq. (49), which leads to the expression

$$\Pi^M_\eta(\omega_n) = -2\Pi^{xx}_{11} + 2\Pi^{xy}_{12} - \frac{3}{2}(\Pi^{yy}_{11} + \Pi^{yx}_{12} + \Pi^{xy}_{21} + \Pi^{xx}_{22}), \tag{50}$$

where the lower indices indicate the components of the Dirac matrices, whereas the upper indices indicate the component of the spatial derivative, see Eq. (20). The last four terms in Eq. (50) obtain contributions only from one-loop diagrams by the same arguments as before, see Eqs. (21) and (22). For the first two terms in Eq. (50) the diagrams containing more than one loop do not vanish. However, the multiloop contributions cancel each other after integration due to the isotropy. Thus we conclude that only one-loop diagrams are contributing to Eq. (50). After carrying out the Matsubara sums and analytical continuation we obtain the retarded correlator, which we write using Eq. (30) as

$$\Pi^R_\eta(\omega) = 2\int\frac{d\boldsymbol{p}}{(2\pi)^3}\Big[p_x^2S_{11} - p_xp_yS_{21} + \frac{3}{4}(p_y^2S_{11} + p_xp_yS_{21} + p_xp_yS_{12} + p_x^2S_{22})\Big], \tag{51}$$

where we have suppressed the $(\boldsymbol{p},\omega)$ arguments of the $S_{\mu\nu}[f=1]$ functions. We obtain the shear viscosity from the Kubo-Zubarev formula (44) by using the relation (35) and the symmetry $p_x \leftrightarrow p_y$

$$\eta = -\frac{\pi}{10}\int_{-\infty}^\infty d\varepsilon\frac{\partial n(\varepsilon)}{\partial\varepsilon}\times\int\frac{d\boldsymbol{p}}{(2\pi)^3}[(2p_x^2+3p_y^2)\mathcal{T}_{11} + p_xp_y\mathcal{T}_{12}], \tag{52}$$

where the $\mathcal{T}_{\mu\nu}$ tensor is defined in Eq. (36). Substituting the decomposition for the spectral function (39) into this expression we obtain

$$\begin{aligned}\eta &= -\frac{2N_cN_f}{5\pi}\int_{-\infty}^\infty d\varepsilon\frac{\partial n(\varepsilon)}{\partial\varepsilon}\int_0^\Lambda\frac{dp}{2\pi^2}p^2\int\frac{d\Omega}{4\pi}\\ &\quad\times[5p_x^2(-A_s^2m^2 + A_0^2\varepsilon^2 - A_v^2p^2) + 4A_v^2p_x^4 + 8A_v^2p_x^2p_y^2]\\ &= \frac{N_cN_f}{15\pi^3T}\int_{-\infty}^\infty d\varepsilon\frac{\partial n}{\partial\varepsilon}\int_0^\Lambda dp\,p^4\\ &\quad\times[5A_s^2(p,\varepsilon)m^2 - 5A_0^2(p,\varepsilon)\varepsilon^2 + A_v^2(p,\varepsilon)p^2].\end{aligned} \tag{53}$$

We conclude that, as in the case of the thermal and electrical conductivities, the knowledge of the Lorentz components of the spectral function completely determines the shear viscosity of quark matter. We note that our expression (53) for the shear viscosity differs from the expressions given in Refs. [32–35], where only the $[T_{12},T_{12}]$ commutator has been considered; our expression contains all possible commutators as indicated above and is consistent with the definition given in Ref. [60].

FIG. 2. Dyson-Schwinger equation for the constituent quark mass. The dashed and solid lines are the bare and dressed propagators, respectively, and $\Gamma = 1$.

III. QUARK SPECTRAL FUNCTION IN THE TWO-FLAVOR NJL MODEL

Equations (42), (43), and (53) provide the general expressions for the transport coefficients in terms of the Lorentz components of the quark spectral function. Further progress requires the knowledge of the specific form of this spectral function in the regime of physical interest, which is determined by the elementary processes that lead to a nonzero imaginary part of the quark self-energy. We turn now to the derivation of these components within the two-flavor NJL model and start with the phase structure of matter predicted by this model.

At nonzero temperature and density the constituent quark mass $m(T,\mu)$ is found to leading $\mathcal{O}(N_c^0)$ order in the $1/N_c$ expansion from a Dyson-Schwinger equation, where the self-energy is taken in the Hartree approximation, see Fig. 2. The mesonic propagator is obtained from the Bethe-Salpeter equation, shown in Fig. 3, which resums contributions from quark-antiquark polarization insertions. The meson masses are obtained as the poles of the propagator in real space-time for $\boldsymbol{p} = 0$. The relevant calculations are reviewed in Appendix A. The behavior of quark and meson masses as functions of density and temperature are shown in Fig. 4 in the cases of explicitly broken chiral symmetry $m_0 \neq 0$ as well as the chiral limit $m_0 = 0$.

As seen from Fig. 4, there is always a nontrivial solution for the quark masses with $m > m_0$ if chiral symmetry is explicitly broken. In the chiral limit, for fixed chemical potential, the quark mass is nonzero below a certain temperature $T \leq T_c = T_{\mathrm{M0}}$ and is strictly zero for $T \geq T_c$. More generally, at sufficiently high densities and temperatures (for example, $T > T_c \simeq 190$ MeV for $\mu = 0$ or $\mu > \mu_c \simeq 330$ MeV for $T = 0$) one finds that chiral symmetry is restored ($m_0 = m = 0$).

The meson masses found from the Bethe-Salpeter equation for the meson propagator are also shown in Fig. 4. At sufficiently low temperatures and densities we find two solutions for the masses of the π and σ mesons.

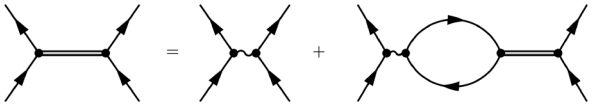

FIG. 3. Bethe-Salpeter equation for mesons: the double lines are the dressed meson propagators.

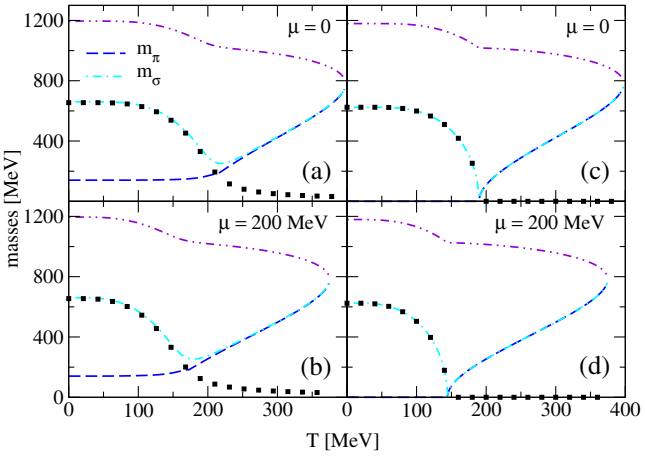

FIG. 4. Quark and meson masses as functions of temperature at chemical potential $\mu = 0$ (upper row) and $\mu = 200$ MeV (lower row). The symbols correspond to twice the quark mass, the dashed and dash-dotted lines correspond to the low-mass mesonic solutions, while the dash-double-dotted lines correspond to the high-mass mesonic solution (see discussion in text). Left panels: $m_0 > 0$, right panels: $m_0 = 0$.

The two low-mass solutions correspond to the masses of the well-known π and σ mesons, and they satisfy numerically the relation $m_\sigma^2 = m_\pi^2 + 4m^2$ within 2% precision. The high-mass solutions are approximately the same for the scalar and pseudoscalar modes and may correspond to a resonance state. Note that in the chiral limit $m_0 = 0$ the low-mass solutions are given by $m_\pi = 0$ and $m_\sigma = 2m$, below the critical temperature T_c for chiral phase transition. Above the critical temperature these solutions become degenerate. As seen from Fig. 4, the lower and upper solutions approach each other with increasing temperature and coincide at a temperature $T_{\max} \simeq 400$ MeV in the case $\mu = 0$. This limiting temperature decreases with increasing chemical potential.

Above $T_{\max}$ no solutions are found for the meson masses anymore, i.e., the mesonic modes exist only for $T \leq T_{\max}$ within the zero-momentum pole approximation for the meson propagator. The maximal temperature of existence of mesons $T_{\max}$ versus chemical potential is shown in Fig. 5. In the limit $T \to 0$ the transition line ends at $\mu_{\max} = \Lambda$, which implies $m_M \to 2\Lambda$.

Another important temperature shown here is the Mott temperature T_{M}, which is defined by the condition $m_\pi = 2m$ in the cases $m_0 = 0$ and $m_0 \neq 0$. Above this temperature $m_\pi > 2m$, and the pion can decay into an on-shell quark-antiquark pair. As seen from Figs. 4 and 5, T_{M} decreases with chemical potential from the value $T_{\mathrm{M}} \simeq 213$ MeV at $\mu = 0$ and vanishes at $\mu \approx 345$ MeV. It coincides with the chiral transition temperature in the chiral limit $m_0 = 0$.

To express the components of the spectral function in terms of the self-energies we write the full quark retarded/advanced Green's function as

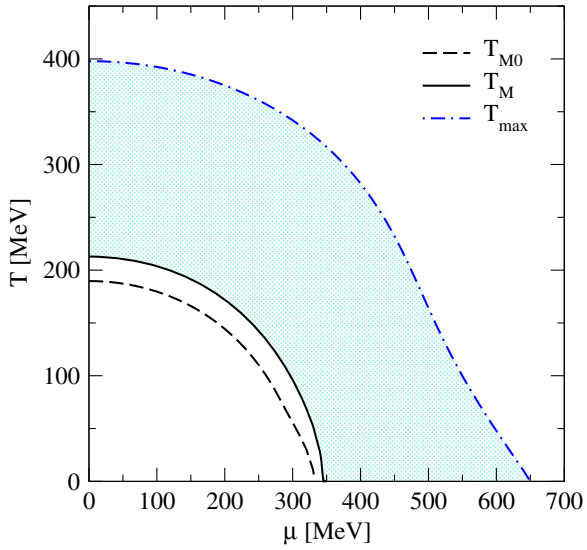

FIG. 5. The Mott temperature $T_{\rm M}$ and the temperature $T_{\rm max}$ (see discussion in the text) as functions of the chemical potential. The dashed line is the Mott temperature in the chiral limit $T_{\rm M0} \equiv T_c$. The shaded area shows the portion of the phase diagram where our computations are applicable.

$$G^{R/A}(p_0,\boldsymbol{p}) = \frac{1}{\not{p} - m - \Sigma^{R/A}(p_0,\boldsymbol{p})}, \tag{54}$$

where $\Sigma^{R/A}$ is the quark-antiquark retarded/advanced self-energy, which in the most general case (due to parity conservation, translational and rotational invariance, as well as time-reversal invariance) can be written in the following form

$$\Sigma^{R(A)} = m\Sigma_s^{(*)} - p_0\gamma_0\Sigma_0^{(*)} + \boldsymbol{p}\cdot\boldsymbol{\gamma}\Sigma_v^{(*)}. \tag{55}$$

According to the definition of the spectral function (29) we find

$$A(p_0,\boldsymbol{p}) = -\frac{1}{\pi}(mA_s + p_0\gamma_0 A_0 - \boldsymbol{p}\cdot\boldsymbol{\gamma}A_v), \tag{56}$$

with

$$A_i = \frac{1}{d}[n_1\varrho_i - 2n_2(1+r_i)], \qquad d = n_1^2 + 4n_2^2, \tag{57}$$

where

$$n_1 = p_0^2[(1+r_0)^2 - \varrho_0^2] - \boldsymbol{p}^2[(1+r_v)^2 - \varrho_v^2] - m^2[(1+r_s)^2 - \varrho_s^2], \tag{58}$$

$$n_2 = p_0^2\varrho_0(1+r_0) - \boldsymbol{p}^2\varrho_v(1+r_v) - m^2\varrho_s(1+r_s), \tag{59}$$

with the short-hand notations $\varrho_i = {\rm Im}\Sigma_i$ and $r_i = {\rm Re}\Sigma_i$, $i = s, 0, v$. From now on we will neglect the irrelevant real parts of the self-energy, which lead to momentum-dependent corrections to the constituent quark mass in next-to-leading order $\mathcal{O}(N_c^{-1})$.

We now consider the quark self-energy that contributes to the transport phenomena because of a nonvanishing imaginary part, closely following similar computations by Refs. [35,36]. The dominant processes, according to the discussion of the phase structure above, are the meson decays into two quarks and the inverse process above the Mott temperature $T_{\rm M}$. The quark self-energy arising from meson exchange is given in Matsubara space by

$$\Sigma^M(\boldsymbol{p},\omega_n) = \quad \begin{matrix} & \boldsymbol{p}-\boldsymbol{q},\omega_n-\omega_m & \\ \Gamma_M & \smile & \Gamma_M \\ & \boldsymbol{q},\omega_m & \end{matrix}$$
$$= T\sum_m \int \frac{d\boldsymbol{q}}{(2\pi)^3}\,[\Gamma_M S(\boldsymbol{q},\omega_m) \times \Gamma_M D_M(\boldsymbol{p}-\boldsymbol{q},\omega_n-\omega_m)]\,, \tag{60}$$

where $S(\boldsymbol{q},\omega_m)$ is the quark propagator with constituent mass, and the index $M = \pi, \sigma$ indicates the meson. Using $\Gamma_\sigma = 1$ and $\Gamma_\pi = i\gamma_5\boldsymbol{\tau}$ we find the decomposition

$$\Sigma^M(\boldsymbol{p},\omega_n) = P_M m\Sigma_s^M + i\omega_n\gamma_0\Sigma_0^M - \boldsymbol{p}\cdot\boldsymbol{\gamma}\Sigma_v^M, \tag{61}$$

where $P_\sigma = 1$, $P_\pi = -1$ and

$$\Sigma_{s,v}^M = g_M^2\int\frac{d\boldsymbol{q}}{(2\pi)^3}\frac{\mathscr{D}_{s,v}}{4E_qE_M} \times\left[\frac{i\omega_n\mathscr{L}_3 - 2E_+\mathscr{L}_1}{E_+^2+\omega_n^2} - \frac{i\omega_n\mathscr{L}_3 + 2E_-\mathscr{L}_2}{E_-^2+\omega_n^2}\right], \tag{62}$$

$$\Sigma_0^M = g_M^2\int\frac{d\boldsymbol{q}}{(2\pi)^3}\frac{\mathscr{D}_0}{4E_qE_M} \times\left[\frac{2i\omega_n\mathscr{L}_1 - E_+\mathscr{L}_3}{E_+^2+\omega_n^2} + \frac{2i\omega_n\mathscr{L}_2 + E_-\mathscr{L}_3}{E_-^2+\omega_n^2}\right], \tag{63}$$

with the short-hand notations

$$\mathscr{L}_1 = 1 + n_B(E_M) - \frac{1}{2}[n^+(E_q) + n^-(E_q)],$$
$$\mathscr{L}_2 = n_B(E_M) + \frac{1}{2}[n^+(E_q) + n^-(E_q)],$$
$$\mathscr{L}_3 = n^+(E_q) - n^-(E_q), \tag{64}$$

and (see Appendix B for details)

$$\mathscr{D}_s = 1, \qquad \mathscr{D}_v = \frac{\boldsymbol{q}\cdot\boldsymbol{p}}{p^2}, \qquad \mathscr{D}_0 = -\frac{E_q}{i\omega_n}. \tag{65}$$

The retarded self-energy is now obtained by analytical continuation $i\omega_n \to p_0 + i\varepsilon$ and has the same Lorentz structure as its Matsubara counterpart. To obtain the quark self-energy one has to take into account the contributions from three pions and one σ-meson. The components of this self-energy sum up as follows

$$\Sigma_s = \Sigma_s^\sigma - 3\Sigma_s^\pi, \qquad \Sigma_{0/v} = -\Sigma_{0/v}^\sigma - 3\Sigma_{0/v}^\pi. \quad (66)$$

For the imaginary part of the on-shell quark self-energy ($\varrho \equiv \mathrm{Im}\Sigma$) one finds

$$\varrho_j^M(p)|_{p_0=E_p} = \frac{g_M^2}{16\pi p}\int_{E_{\min}}^{E_{\max}} dE\mathcal{T}_j[n_B(E_M) + n^-(E)], \quad (67)$$

where $j = s, 0, v$, $E_M = E + E_p$, and

$$\mathcal{T}_s = 1, \quad \mathcal{T}_v = \frac{m_M^2 - 2m^2 - 2EE_p}{2p^2}, \quad \mathcal{T}_0 = -\frac{E}{E_p}. \quad (68)$$

The distribution function for quarks and antiquarks is defined as $n^\pm(E) = [e^{\beta(E\mp\mu)} + 1]^{-1}$, and $n_B(E) = (e^{\beta E} - 1)^{-1}$ is the Bose distribution function for zero chemical potential. In the same way we find for the antiquark on-shell self-energy ($p_0 = -E_p$)

$$\varrho_j^M(p)|_{p_0=-E_p} = -\frac{g_M^2}{16\pi p}\int_{E_{\min}}^{E_{\max}} dE\mathcal{T}_j[n_B(E_M) + n^+(E)], \quad (69)$$

where

$$E_{\min,\max} = \frac{1}{2m^2}\left[(m_M^2 - 2m^2)p_0 \pm pm_M\sqrt{m_M^2 - 4m^2}\right]. \quad (70)$$

The range of integration is according to Eq. (70)

$$E_{\max} - E_{\min} = \frac{pm_M}{m^2}\sqrt{m_M^2 - 4m^2}. \quad (71)$$

We note that if $m_M \geq 2m$ the integration range is not empty. If $m = 0$, we have

$$E_{\min} = \frac{m_M^2}{4p}, \qquad E_{\max} \to \infty. \quad (72)$$

The full quark-antiquark self-energy in on-shell approximation can be written as

$$\varrho_j(p_0, p) = \theta(p_0)\varrho_j^+(p) + \theta(-p_0)\varrho_j^-(p), \quad (73)$$

with $\varrho_j^\pm(p) = \varrho_j(p_0 = \pm E_p, p)$. It is seen from Eqs. (67) and (69) that ϱ^+ and ϱ^- are related by the relation $\varrho_j^-(\mu, p) = -\varrho_j^+(-\mu, p)$, therefore

$$\begin{aligned}\varrho_j(\mu, -p_0, p) &= \theta(-p_0)\varrho_j^+(\mu, p) + \theta(p_0)\varrho_j^-(\mu, p)\\ &= -\theta(-p_0)\varrho_j^-(-\mu, p) - \theta(p_0)\varrho_j^+(-\mu, p)\\ &= -\varrho_j(-\mu, p_0, p), \end{aligned} \quad (74)$$

where we indicated the μ-dependence of the self-energy explicitly.

Now for any transport coefficient $\chi(\mu)$ we can write

$$\chi(\mu) = \int_{-\infty}^{\infty} d\varepsilon n^+(\varepsilon)[1 - n^+(\varepsilon)]\int_0^\Lambda dp\mathcal{F}(p, \varepsilon, \mu), \quad (75)$$

where $\mathcal{F}(p, \varepsilon, \mu) \equiv \mathcal{F}(p, \varepsilon, h(\mu), \varrho_j(\mu, \varepsilon, p))$ is an even function of p and ϱ_j, as seen from Eqs. (42), (43), (53), and (57)–(59). It is invariant under the inversion $\varepsilon \to -\varepsilon$ in the cases of the electrical conductivity and the shear viscosity, and under the simultaneous inversions $\varepsilon \to -\varepsilon$, $h \to -h$ in the case of the thermal conductivity. Because h is an odd function of the chemical potential, see Appendix C, it follows from Eq. (74) that ($\varepsilon \equiv p_0$)

$$\begin{aligned}\mathcal{F}(p, -\varepsilon, \mu) &= \mathcal{F}(p, -\varepsilon, h(\mu), \varrho_j(\mu, -\varepsilon, p))\\ &= \mathcal{F}(p, \varepsilon, -h(\mu), -\varrho_j(-\mu, \varepsilon, p))\\ &= \mathcal{F}(p, \varepsilon, h(-\mu), \varrho_j(-\mu, \varepsilon, p))\\ &= \mathcal{F}(p, \varepsilon, -\mu).\end{aligned}$$

Using this property in combination with relations $n^+(\mu, -\varepsilon) = 1 - n^-(\mu, \varepsilon)$, $n^-(\mu, \varepsilon) = n^+(-\mu, \varepsilon)$, and employing Eq. (73) we rewrite Eq. (75) as

$$\chi(\mu) = \chi^+(\mu) + \chi^-(\mu), \quad (76)$$

where we separated the contributions from positive and negative energies

$$\chi^+(\mu) = \int_0^\infty d\varepsilon n^+(\mu, \varepsilon)[1 - n^+(\mu, \varepsilon)] \times \int_0^\Lambda dp\mathcal{F}(p, \varepsilon, \varrho_j^+(\mu, p)), \quad (77)$$

$$\chi^-(\mu) = \int_{-\infty}^0 d\varepsilon n^+(\mu, \varepsilon)[1 - n^+(\mu, \varepsilon)] \times \int_0^\Lambda dp\mathcal{F}(p, \varepsilon, \varrho_j^-(\mu, p)) = \chi^+(-\mu). \quad (78)$$

Therefore from Eq. (76) we obtain

$$\chi(\mu) = \chi^+(\mu) + \chi^+(-\mu), \quad (79)$$

which implies that the transport coefficients are even functions of the chemical potential, as expected.

IV. NUMERICAL RESULTS

A. Self-energies and spectral functions

The imaginary parts of the quark and antiquark on-shell self-energies, given by Eqs. (67) and (69), respectively, are shown in Fig. 6 as functions of the quark momentum p at fixed values of the temperature and the chemical potential. For each value of μ the temperature values are chosen to cover the range $T_{\rm M} < T < T_{\rm max}$, as displayed in Fig. 5. Below $T_{\rm M}$, which is defined by the continuum condition $m_\pi = 2m$, the imaginary parts of the on-shell self-energies of quarks are negligible, since the processes of quark scattering with meson exchange are kinematically forbidden in the case of π-mesons, and are strongly suppressed in the case of σ-mesons if compared to off-shell processes.

The three components of the self-energies differ by the factors $\mathcal{T}_j$. As in the case of the scalar self-energy $\mathcal{T}_s = 1$, we conclude that the differences seen between the components ϱ_j in Fig. 6, as for example the sign change between ϱ_s and ϱ_0 and more pronounced maxima in ϱ_0 and ϱ_v than in ϱ_s, originate from the $\mathcal{T}_j$ factors in Eq. (68). To understand the small-p behavior of the self-energies, note first that the explicit p^{-1} divergence in Eqs. (67) and (69) is cancelled by the linear-in-p dependence of the integration range, given by Eq. (71). Furthermore, when $p \to 0$ the limits of integration tend to $(m_M^2 - 2m^2)/2m$, see Eq. (70). If this limiting value is comparable to the temperature, then the quark and antiquark distribution functions are nonzero and contribute to the self-energies for $p \to 0$; this is the case in Figs. 6(a), 6(d), and 6(g). In case where $(m_M^2 - 2m^2)/2m \gg T$ the small-p contributions are suppressed by the vanishingly small distribution functions, see Figs. 6(b), 6(e), and 6(h), as well as 6(c), 6(f), and 6(i). However, in the chiral limit $m_0 = 0$ we always find the asymptotic behavior $\mathrm{Im}\Sigma \to 0$, when $p \to 0$, because the lower bound of the integral (67) becomes infinitely large as seen from Eq. (72).

In the large-p limit the integration range is broad and the asymptotics is controlled by the cutoff of high-momentum contributions by the distribution functions, as well as the factors $\mathcal{T}_j$. Thus the appearance of the maxima in the self-energies [necessarily in the case $(m_M^2 - 2m^2)/2m \gg T$] is the consequence of this asymptotic behavior. The shifts of the maxima to higher momenta with increasing temperature is caused by the shift in energy sampling of the distribution functions.

Next we examine the self-energies at fixed chemical potential, i.e., the vertical columns in Fig. 6. Because the difference $m_M - 2m$ increases with temperature as we move away from the Mott line the integration region increases. At the same time the distribution functions cover phase space with higher energies. In combination this leads to an increase of the imaginary parts of self-energies of

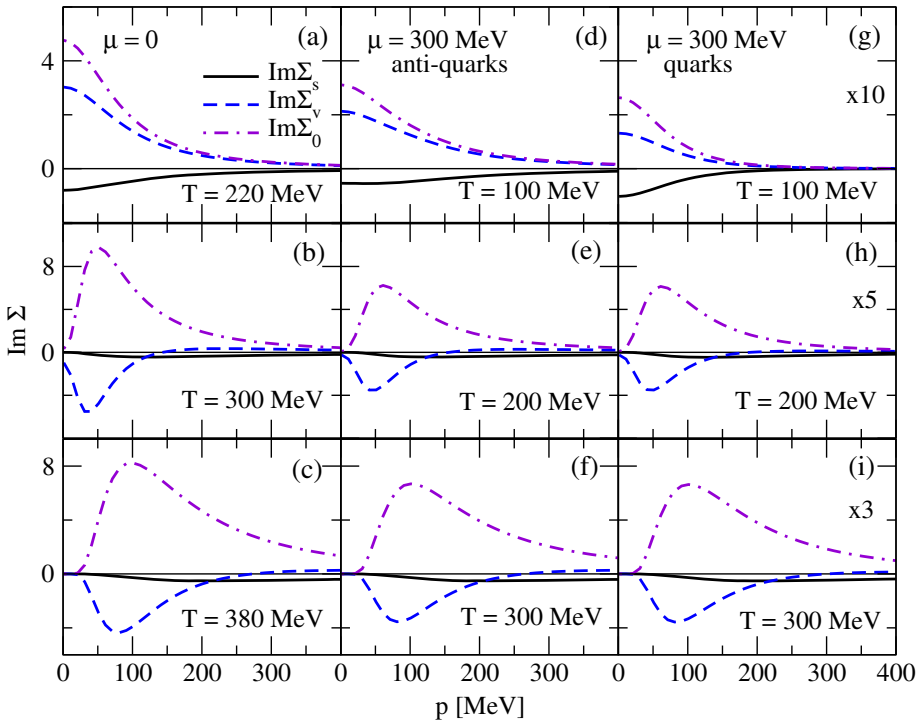

FIG. 6. The imaginary parts of the three Lorentz components of the quark and antiquark on-shell self-energies as functions of momentum at various values of temperature and chemical potential. The signs of the antiquark self-energies have been inverted.

quarks and antiquarks with temperature, which is well pronounced for high momenta. This increase is also caused by the additional temperature dependence of the coupling constant g_M, see Fig. 16 in Appendix A.

Consider now the dependence of the self-energies on the chemical potential for fixed temperature by comparing, for example, Figs. 6(a), 6(e), and 6(h) with 6(b), 6(f), and 6(i). We observe two effects: (i) the contributions to the self-energies from large p becomes larger for $\mu \neq 0$ both for quarks and antiquarks; (ii) the overall magnitude of the quark self-energies (for example the maximum) is reduced for $\mu \neq 0$. Nonzero μ affects quark self-energies stronger than that of antiquarks because of a stronger depletion of the antiquark population at nonzero baryon density, on which the quark self-energy depends. In fact, at any temperature the quark self-energies are by a factor of two smaller than their antiquark counterparts for $\mu = 200$ MeV and this difference grows for large μ; e.g., for $\mu = 300$ MeV the suppression factor is ten at $T = 100$ MeV. A similar comparison for antiquarks [see Figs. 6(a)–6(c) and 6(d)–6(f)] shows that the antiquark self-energies at nonzero μ are comparable to the self-energies for the $\mu = 0$ case.

Next we turn to the three Lorentz components of the spectral function given by Eqs. (56)–(59), which are shown in Fig. 7 as functions of the quark momentum at three values of the quark (off-shell) energy, $\varepsilon_1 = 100$, $\varepsilon_2 = 300$, and $\varepsilon_3 = 500$ MeV. The quasiparticle peak in the spectral functions appears for $p \simeq \varepsilon$, as expected from Eqs. (58). An estimate gives $n_1 \approx (p_0^2 - p^2)(1 - \varrho_{0,v}^2)$ and $n_2 \approx (p_0^2 + p^2)\varrho_0$, therefore the denominator d attains its minimum roughly at $p \simeq p_0$. In all cases it is seen that the heights of the peaks increase with the quark energy. As expected on physical grounds, the quasiparticle peaks are broadened with increasing temperature and are replaced by more complex structures in the high-temperature regime, see Figs. 7(c), 7(f), and 7(i).

A comparison of quark and antiquark spectral functions shows that the quasiparticle peaks of quarks are sharper than that of antiquarks for the same temperature and chemical potential. As indicated in Fig. 7, for $\mu = 300$ MeV the peak in the spectral function of quarks is by a factor of 10^2 larger than that of antiquarks at $T = 100$ MeV and by factor of ten at $T = 200$ MeV. Finally note that the temporal and vector components of the spectral function are of the same order of magnitude and are almost coinciding at high energies, whereas the scalar component is always suppressed. Thus, we may already conclude that the main contribution to the transport coefficients will originate from the temporal and vector components of the spectral functions. Note that the vector component of the imaginary self-energy energy changes the sign, consequently the corresponding spectral function changes its sign as well. However, the overall spectral

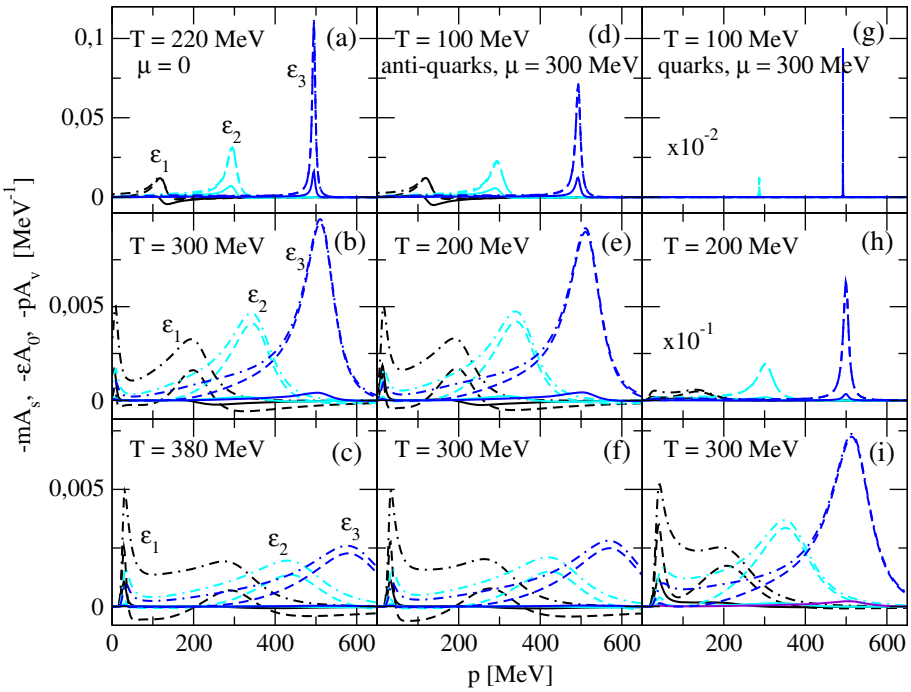

FIG. 7. Dependence of three Lorentz components of the quark and antiquark spectral functions $-mA_s$ (solid line), $-\varepsilon A_0$ (dash-dotted line) and $-pA_v$ (dashed line) on the momentum. Figures (a)–(c) correspond to $\mu = 0$, (d)–(f) to antiquarks with $\mu = 300$ MeV, and (g)–(i) to quarks with $\mu = 300$ MeV. These spectral functions are shown at three energies $\varepsilon_1 = 100$, $\varepsilon_2 = 300$, and $\varepsilon_3 = 500$ MeV, as indicated in the plot. Note that the vector component of the spectral function changes its sign, whereas the remaining components do not, see the discussion in the text.

width of the quasiparticles, which defines their decay rate and contains the contributions from all Lorentz components remains positive [36].

B. Thermal and electrical conductivities

We now turn to the evaluation of the thermal and electrical conductivities as given by Eqs. (42) and (43). Before discussing the numerical results, consider the generic structure of these expressions. For a given value of ε the inner integrand has a peak structure with a maximum located at $p \simeq \varepsilon$, as implied by the shape of the spectral functions. The heights of the peaks rapidly increase with ε. As a consequence, the inner momentum integral in Eqs. (42) and (43) is a rapidly increasing function of $|\varepsilon|$ as long as $|\varepsilon| \leq \Lambda$. For energies larger than Λ the peaks are outside of the integration range (because of the momentum cutoff) and the integral sharply decreases with ε. The outer integration contains the factor $\partial n(\varepsilon)/\partial\varepsilon$ which at low temperatures is strongly peaked at the energy $\varepsilon = \mu$. At high temperature it transforms into a broad, bell-shaped structure which samples energies far away from μ.

It is evident from Eqs. (42) and (43) that for $\mu \to 0$ the integrands of the momentum integrals are even functions of ε, as discussed above, and the quark and antiquark contributions originating from positive and negative ranges of the ε-integration are equal. At nonzero chemical potentials the contribution of antiquarks is suppressed by both spectral functions and by the factor $\partial n/\partial\varepsilon$. We will give an explicit numerical example below in Fig. 10.

Figure 8 shows the temperature dependence of κ and σ for several values of the chemical potential. The conductivities decrease with temperature for all values of the chemical potential. The observed decrease is the result of the broadening of the spectral functions with temperature, which physically corresponds to stronger dispersive effects and shorter relaxation times. This implies smaller conductivities.

Note that at the Mott temperature and below the conductivities become very large because the dispersive effects incorporated in the spectral functions via the imaginary parts of the self-energies vanish for pions and are very small for the σ-meson. This is the consequence of the on-shell approximation, and can be improved if one incorporates off-shell contributions to the self-energies. This improvement close to (and below) the Mott temperature that incorporates off-shell kinematics is unimportant at temperatures already slightly above the Mott temperature, where the transport coefficients are described by on-shell kinematics quite well. (For a computation of off-shell self-energies see Ref. [35], where their impact for the shear viscosity were found to be small.)

Comparing the overall behavior of the thermal and electrical conductivities we observe two main differences:

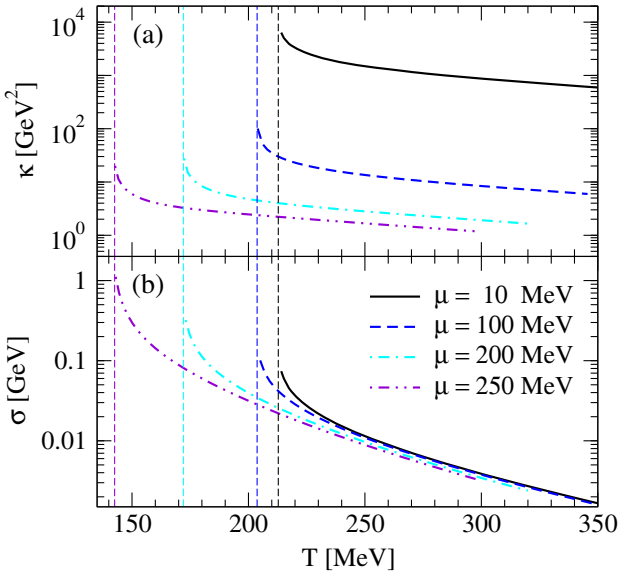

FIG. 8. The temperature dependence of (a) thermal and (b) electrical conductivity at various values of the chemical potential. The vertical lines show the Mott temperature at the given value of μ.

(i) the electrical conductivity drops faster with temperature than the thermal conductivity, (ii) for small chemical potentials the thermal conductivity diverges, whereas the electrical conductivity remains almost independent of the chemical potential. Both effects originate from those terms in Eq. (42) for κ which contain the enthalpy h. In the relevant temperature-density range, the minimal value of the enthalpy per particle is $h_{\rm min} \simeq 0.8$ GeV, see Fig. 18 in Appendix C. This value already exceeds the cutoff parameter $\Lambda \simeq 0.65$ GeV, which is the characteristic energy scale of the model, therefore one may conclude that the dominant terms in κ are the terms containing h, i.e., the terms arising from the second and third correlators on the right-hand side of Eq. (11). The enthalpy per particle rapidly increases with the decrease of the chemical potential, therefore at small chemical potentials the main contribution comes from the third term. Numerically we find that the first two terms are negligible compared to the third one for $\mu \leq 100$ MeV. The second correlator becomes important once $\mu \geq 100$ MeV, whereas the first one is always suppressed for $\mu \leq 250$ MeV. Thus, using Eqs. (5), (6), (11), and (34), we obtain for small chemical potentials $\mu \leq 100$ MeV a simple relation between thermal and electrical conductivities

$$\frac{\kappa}{\sigma} = \frac{N_f}{\mathrm{Tr}\hat{Q}^2}\frac{h^2}{T} = \frac{9h^2}{10\pi\alpha T}. \tag{80}$$

Note that the first equality holds for any number of flavors, whereas in the second step we substituted $N_f = 2$. For $\mu \ll T$ we have the asymptotic behavior $h \simeq 7\pi^2T^2/15\mu$,

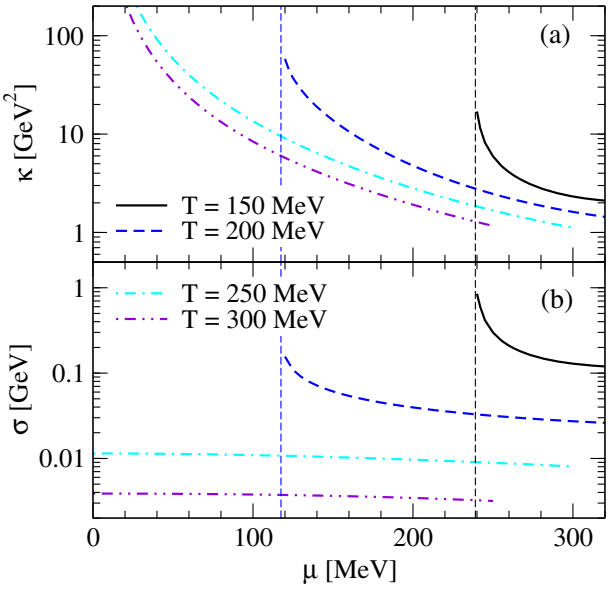

FIG. 9. The dependence of (a) thermal and (b) electrical conductivity on the chemical potential at various temperatures. The vertical lines show the value of the chemical potential where the temperature approaches the Mott temperature.

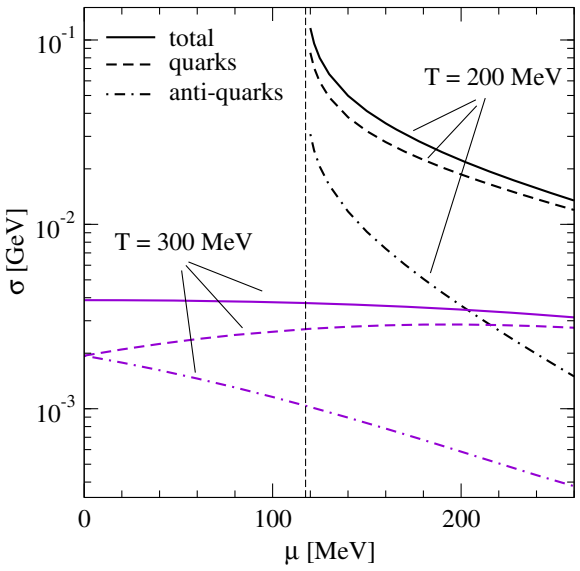

FIG. 10. The partial contributions of quarks and antiquarks to the electrical conductivity and their sum as functions of the chemical potential at two temperatures indicated in the plot.

therefore the thermal conductivity diverges at vanishing baryon density as $\kappa \propto \mu^{-2}$ [43]. Substituting the expression for h in Eq. (80) we find in the nondegenerate regime

$$\frac{\kappa\mu^2}{\sigma T^3} = \frac{N_f}{\mathrm{Tr}\hat{Q}^2}\left(\frac{7\pi^2}{15}\right)^2 = \frac{49\pi^3}{250\alpha} \simeq 830. \tag{81}$$

It is seen that the Wiedemann-Franz law $\sigma T/\kappa \sim$ const. does not hold in this case. Finally, we note that away from the Mott line we have the scalings $\sigma \propto T^{-6}$ and $\kappa \propto T^{-\gamma}$ with $\gamma = 3$ for $\mu \leq 100$ MeV and $\gamma = 2$ for $\mu \geq 200$ MeV.

The dependence of conductivities on the chemical potential is shown in Fig. 9. The electrical conductivity is seen to be nearly independent of the chemical potential away from the Mott transition line. Only close to this transition σ increases because of the vanishing of the spectral width at T_{M}. Note that for temperatures $T \geq 250$ MeV the electrical conductivity remains almost constant because of the absence of the Mott line at these temperatures. However, the thermal conductivity is always a rapidly decreasing function of the chemical potential because of the reasons discussed above, and becomes infinitely large in the limit $\mu \to 0$.

At nonzero μ the symmetry between quarks and antiquarks is broken; its consequences discussed above are illustrated in Fig. 10, where the quark and antiquark contributions to σ are shown separately. At temperatures close to T_{M} both contributions decrease with quarks contributing dominantly. For temperatures away from the Mott transition line, the moderate increase in the conductivity of quarks up to $\mu \simeq 200$ MeV is accompanied by a rapid decrease in the contribution of antiquarks, which becomes negligible at $\mu > 200$ MeV. The sum of these two contributions turns out to be a slowly decreasing function of μ in the entire range of μ and T, see Fig. 9.

In order to remove the effect of the variations of the position of the Mott line with the chemical potential, we show in Fig. 11 again the conductivities as in Fig. 8, but with the temperature axis scaled by the corresponding $T_{\mathrm{M}}(\mu)$. In this case the conductivities display a universal

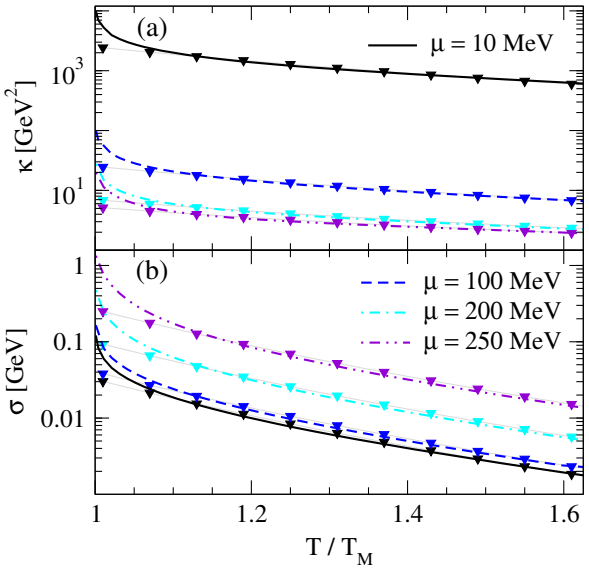

FIG. 11. The thermal conductivity κ (a) and electrical conductivity σ (b) as functions of the scaled temperature T/T_{M} at several values of the chemical potential.

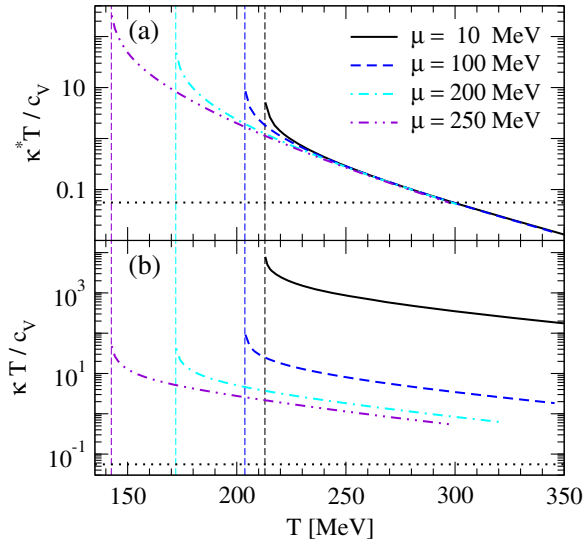

FIG. 12. The ratios $\kappa^* T/c_V$ (a) and $\kappa T/c_V$ (b) as functions of the temperature at several values of the chemical potential.

dependence on this scaled temperature, their values being only shifted by a μ-dependent constant.

Apart from the Wiedemann-Franz relation, the ratios the $\kappa T/c_V$ and $\kappa^* T/c_V$ are of interest. Here κ^* is defined by Eq. (42) with $h = 0$ and c_V is the specific heat capacity as defined in Appendix C. These ratios are shown in Fig. 12.

We conjecture that the ratio $\kappa^* T/c_V$, which is associated with the energy transfer, is bounded from below due to the quantum mechanical uncertainty principle. To motivate this conjecture we refer to kinetic theory of noninteracting gases. Because for temperatures $T > T_M$ the quark masses are negligible compared to other scales, we can set their average velocity $\bar{v} \simeq 1$. Furthermore, in this regime the characteristic energy $\varepsilon \simeq 3T$. Now, according to the kinetic theory of dilute gases the thermal conductivity is estimated as

$$\kappa^{\rm kin} \simeq \frac{1}{3} c_V \bar{v} l \simeq \frac{1}{3} c_V \tau, \tag{82}$$

where l is the mean free path and $\tau = l/\bar{v}$ is the mean collision time. Therefore, we find that at high temperatures $\kappa T/c_V \simeq T\tau/3 \simeq \varepsilon\tau/9$. Because of the uncertainty principle $\varepsilon\tau \geq 1/2$, we find the following bound (recovering the natural constants)

$$\frac{\kappa^{\rm kin} T}{c_V} \geq \frac{\hbar c^2}{18 k_B}. \tag{83}$$

In the present context $\kappa^{\rm kin}$ in Eq. (83) should be associated with κ^* because this quantity serves as the analogue of the thermal conductivity defined in the kinetic theory of gases. Indeed, both quantities involve the total energy transport and do not separate the convective particle current which is excluded from κ by definition.

Note that in the case of shear viscosity the discussion of an analogous bound was given by Ref. [43] and a more stringent limit (the so-called KSS bound) was suggested later on from gauge-gravity duality considerations [53].

According to panel (a) of Fig. 12 the bound (83) is violated for the ratio involving κ^* at high temperatures $T > 300$ MeV. It is remarkable that this occurs in the same range where the shear-viscosity bound is violated (see below, Sec. IV C). The inclusion of gluonic degrees of freedom will mitigate this violation. The quark-meson exchange processes will not be the most dominant processes away from the Mott temperature and the gluonic degrees of freedom are expected to play a significant role in thermal transport.

C. Shear viscosity

The shear viscosity of quark matter has been studied extensively because of the experimental evidence for its very low value in heavy-ion collisions where quark-matter formation is expected and because of the conjectured universal lower bound of the ratio η/s derived from gauge-gravity duality. We now evaluate the expression for η given by Eq. (53) and compare it to earlier studies, in particular those based on the two-flavor NJL model.

Figure 13 shows the temperature dependence of the shear viscosity and the ratio η/s. The entropy density of the present model is discussed in Appendix C. As in the case of the conductivities, the shear viscosity is a decreasing function of the temperature, for the reasons already explained in detail above: the dispersive effects increase

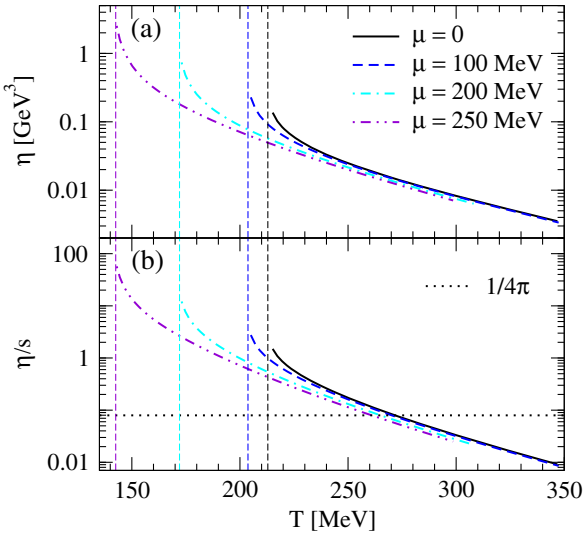

FIG. 13. The temperature dependence of the shear viscosity η (a) and its ratio to the entropy density (b) at various values of the chemical potential. The vertical lines show the Mott temperature at the given value of μ.

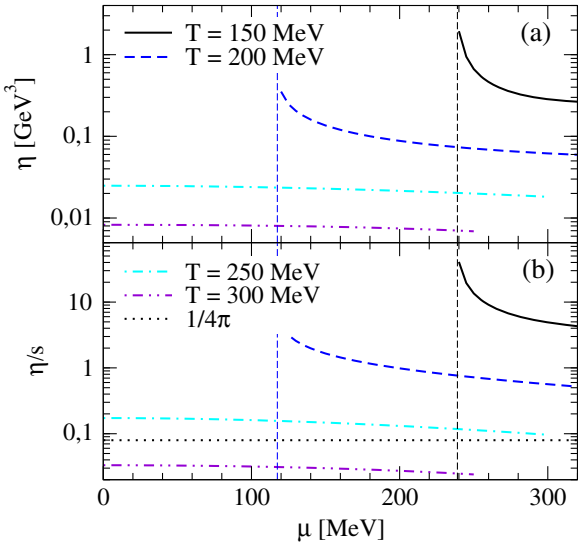

FIG. 14. The dependence of the shear viscosity (a) and the ratio η/s (b) on the chemical potential at various temperatures. The vertical lines show the value of the chemical potential where the temperature approaches the Mott temperature.

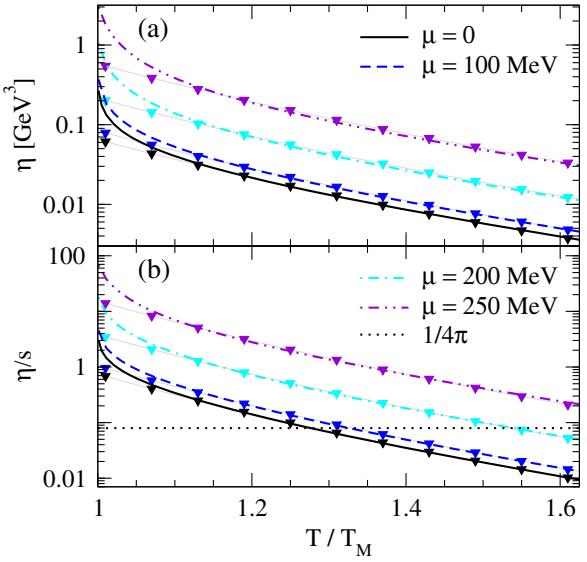

FIG. 15. The shear viscosity (a) and the ratio η/s (b) as functions of the scaled temperature T/T_{M} at several values of the chemical potential.

with the temperature and the viscosity of matter is reduced. The entropy density of quark matter is an increasing function of temperature (linear in the degenerate regime $T \ll \mu$ and cubic in the nondegenerate regime $T \gg \mu$), therefore the ratio η/s decreases faster than η with increasing temperature. In the high-temperature regime η and η/s have the scaling T^{-6} and T^{-9}, respectively. The enhancement of both quantities as $T \to T_{\mathrm{M}}$ is understood as due to vanishing of the relevant on-shell self-energies at the Mott temperature. At high temperatures $T \gtrsim 270$ MeV the ratio η/s undershoots the KSS bound $1/4\pi$ [53]. This is an indication of the change in the processes that dominate the viscosity, namely from quark-meson fluctuations to those including gluonic degrees of freedom, which are integrated out from the NJL model. Their contribution becomes increasingly important at high temperatures and leads to an increase of the viscosity with temperature, see Refs. [24,25,39,62].

The dependence of η and η/s on the chemical potential is shown in Fig. 14. As in the case of the electrical conductivity, these are slowly decreasing functions of μ at fixed temperature except at the corresponding Mott line where η formally diverges. Finally, in Fig. 15 we show these quantities as functions of the ratio T/T_{M}. As in the case of the conductivities, we observe a universal behavior of η and η/s on T/T_{M} for fixed μ values, i.e., the curves belonging to different values of μ are only shifted vertically by a μ-dependent constant.

D. Fitting transport coefficients

The observed nearly universal behavior of the transport coefficients with the scaled temperature T/T_{M} for fixed values of the chemical potential suggests fitting transport coefficients as functions of T/T_{M} and the chemical potential, as displayed in Figs. 11 and 15.

For this purpose we first fit the Mott temperature, displayed in Fig. 5, with the formula

$$T_{\mathrm{M}}^{\mathrm{fit}}(\mu) = T_0 \begin{cases} 1 - \sqrt{\gamma y} e^{-\pi/(\gamma y)} & 0 \le y \le 0.5, \\ \sqrt{1.55(1-y) + 0.04(1-y)^2} & 0.5 < y \le 1, \end{cases} \tag{84}$$

with $T_0 = T_{\mathrm{M}}(\mu = 0) = 213$ MeV, $y = \mu/\mu_0$, where $\mu_0 = 345$ MeV corresponds to the point where $T_{\mathrm{M}} = 0$ and the chemical potential attains its maximum on the Mott line, and $\gamma = 2.7$. The formula (84) has relative accuracy $\lesssim 3\%$ for chemical potentials $\mu \le 320$ MeV.

Next, all transport coefficient can be fitted with a generic formula

$$\chi_{\mathrm{fit}} = C\left(\frac{T}{T_{\mathrm{M}}}\right)^{-\alpha} \exp[a_1 y^2 + a_2 y^4 + a_3 y^6] \times \chi_{\mathrm{div}}, \tag{85}$$

where $\chi_{\mathrm{fit}} \in \{\sigma, \kappa, \kappa^*, \eta, \eta/s\}$. The term χ_{div} is diverging in the limit $\mu \to 0$ in the case of κ and is given by the formula

$$\chi_{\mathrm{div}} = \left(\frac{T}{T_{\mathrm{M}}}\right)^2 + y^{-2}. \tag{86}$$

For all other coefficients $\chi_{\mathrm{div}} = 1$. The values of the constants in formula (85) are given in Table I (for each transport coefficient C is given in relevant units). A comparison between the exact results and the fits is shown

TABLE I. The values of the fit parameters in Eq. (85).

$\chi_{\rm fit}$	C	α	a_1	a_2	a_3
σ	0.032	6	2.64	1.23	2.67
κ	2.10	3	−0.95	1.27	0.0
κ^*	1.55	7	3.47	1.08	3.34
η	0.065	6	2.92	0.95	2.7
η/s	0.75	9	3.89	1.72	3.47

in Figs. 11 and 15, where an excellent agreement is observed for temperatures above $T/T_{\rm M} \geq 1.1$. In this domain all fit formulas have relative accuracy $\leq 10\%$.

V. CONCLUSIONS

In this work we have studied the electrical and thermal conductivities as well as provided an update on the shear viscosity of quark matter within the two-flavor NJL model using the Kubo-Zubarev formalism [21,22]. We have derived Kubo formulas for the electrical and thermal conductivities of a relativistic quark plasma taking into account the full Lorentz structure of the self-energies (spectral functions) of the quarks. The two-point correlation functions are evaluated with the full propagator and within the $1/N_c$ approximation to the multiloop contributions; these then imply that vertex corrections are suppressed and the leading-order contributions to the correlation functions arise from single-loop diagrams. It is worthwhile to note that our Kubo formulas for the conductivities have generic validity and can be applied in the broader context of field theories of relativistic plasmas, in a straightforward manner when the vertex corrections are suppressed by some mechanism. We have also revised the corresponding Kubo formula for the shear viscosity.

We have applied this general formalism to compute the electrical and thermal conductivities of the NJL model for quark matter in the regime where the dispersive effects arise from quark-meson scattering above the Mott temperature for dissolution of mesons into quarks. We find that the conductivities are decreasing functions of temperature at fixed chemical potential; they show nearly universal behavior when temperature is scaled by the Mott temperature, i.e., as functions of $T/T_{\rm M}$. We find that the ratio κ/σ does not follow the Wiedemann-Franz law. We then moved on to recompute the shear viscosity of the model with our derived Kubo formula; we find a qualitative agreement with previous results of Refs. [32–35]. In particular the ratio of η/s tends to the KSS bound $1/4\pi$ [53] but undershoots this bound at some intermediate temperature and fails to describe the high-temperature limit where gluonic degrees become important. We have also conjectured a lower bound on the ratio $\kappa^* T/c_V > 1/18$. This conjecture needs further studies from different standpoints, including those well suited for nonperturbative calculations. Within the NJL model we find that this ratio undershoots the lower bound $1/18$ at high temperature predicted by the uncertainty principle.

We have provided simple fit formulas for the electrical and thermal conductivities as well as the shear viscosity with a good relative accuracy, which can be utilized in numerical simulations of hydrodynamics of the quark plasma.

The present work can be expanded in a number of ways by extending the Lagrangian (1) of the model. The role of the confinement can be assessed by extending the NJL model to include the Polyakov loop at finite temperature. The mesons, which appear in the present model as scatterers, can carry momentum and charge in heavy ion experiments and can contribute to transport, as established in numerical simulations of such experiments (see Refs. [39–42] and references therein). In addition, having an access to the spectral functions of quarks, will allows us to compute the rates of the photon and dilepton emission from quark matter in the present model, which is again of interest for the description of heavy ion collisions.

ACKNOWLEDGMENTS

A. H. acknowledges support from the Helmholtz Graduate School for Hadron and Ion Research (HGS-HIRe) at Frankfurt University. A. S. is supported by the Deutsche Forschungsgemeinschaft (Grant No. SE 1836/3-2) and by the Helmholtz International Center for FAIR. We acknowledge the support by NewCompStar COST Action MP1304.

APPENDIX A: DETAILS OF THE NJL-MODEL CALCULATIONS

The constituent quark mass m is found from the gap equation, which to leading order $\mathcal{O}(N_c^0)$ is given by the Hartree approximation (see Fig. 2) and analytically reads

$$S_0^{-1} = S^{-1} - G\langle\bar{\psi}\psi\rangle, \tag{A1}$$

where $S_0^{-1} = \not{p} - m_0$, $S^{-1} = \not{p} - m$ are the free and interacting quark propagators. The quark condensate $\langle\bar{\psi}\psi\rangle$, represented by the loop in diagram Fig. 2, is given by

$$\langle\bar{\psi}\psi\rangle = T\sum_{m\in Z}\int\frac{d\boldsymbol{p}}{(2\pi)^3}\mathrm{Tr}[S(\boldsymbol{p},\omega_m)], \tag{A2}$$

where the summation is over the fermionic Matsubara frequencies $\omega_m = (2m+1)\pi T - i\mu$. The trace is over Dirac, color, and flavor space and the quark propagator is given by

$$S(\boldsymbol{p},\omega_m) = \frac{\Lambda_p^+\gamma_0}{i\omega_m - E_p} + \frac{\Lambda_p^-\gamma_0}{i\omega_m + E_p}, \tag{A3}$$

where Λ_p^+ and Λ_p^- are the projection operators onto positive and negative energy states

$$\Lambda_p^{\pm} = \frac{E_p\gamma_0 \mp \boldsymbol{\gamma}\cdot\boldsymbol{p} \pm m}{2E_p}\gamma_0. \tag{A4}$$

Substituting Eqs. (A3) and (A4) into Eq. (A2) and performing the Matsubara sums we obtain

$$\langle\bar{\psi}\psi\rangle = -4N_cN_f m I_1, \tag{A5}$$

where we defined

$$I_1 = \frac{1}{4\pi^2}\int_0^{\Lambda} dp\,\frac{p^2}{E_p}[1 - n^+(E_p) - n^-(E_p)]. \tag{A6}$$

From Eqs. (A1) and (A5) follows

$$m = m_0 + 4GN_cN_f m I_1. \tag{A7}$$

If $m_0 \neq 0$, Eq. (A7) always has a nontrivial solution $m > m_0$. If $m_0 = 0$, there is a trivial solution $m = 0$, but Eq. (A7) may have nontrivial solutions satisfying

$$4GN_cN_f I_1 = 1. \tag{A8}$$

In this case the vacuum energy is minimized by the solution with the largest m [20]. At high densities and temperatures ($T > T_c \simeq 190$ MeV for $\mu = 0$ or $\mu > \mu_c \simeq 332$ MeV for $T = 0$) Eq. (A8) does not have solutions anymore, and we find that chiral symmetry is restored with $m_0 = m = 0$.

The meson propagators are obtained from the Bethe-Salpeter equation, shown in Fig. 3,

$$D_M = G + G\Pi_M D_M = \frac{G}{1 - G\Pi_M}, \tag{A9}$$

where the quark-antiquark polarizations for the σ-meson and pion $\Pi_M, M = \sigma, \pi$ are given by the formula

$$\Pi_M(\boldsymbol{p},\omega_n) = -T\sum_{m\in Z}\int\frac{d\boldsymbol{q}}{(2\pi)^3}\mathrm{Tr}[\Gamma_M S(\boldsymbol{q}+\boldsymbol{p},\omega_m+\omega_n) \times \Gamma_M S(\boldsymbol{q},\omega_m)] \tag{A10}$$

with $\Gamma_\sigma = 1$, $\Gamma_\pi = i\gamma_5\tau_j$, $j = 1, 2, 3$. From Eq. (A3) we obtain

$$\Pi_M(\boldsymbol{p},\omega_n) = -\int\frac{d\boldsymbol{q}}{(2\pi)^3}\sum_{\pm\pm}\mathcal{T}_M^{\pm\pm}\mathcal{S}^{\pm\pm}, \tag{A11}$$

where we defined

$$\mathcal{T}_M^{\pm\pm} = \mathrm{Tr}[\Gamma_M\Lambda^{\pm}_{q+p}\gamma_0\Gamma_M\Lambda^{\pm}_q\gamma_0], \tag{A12}$$

$$\mathcal{S}^{\pm\pm} = T\sum_m\frac{1}{(i\omega_m + i\omega_n - E^{\pm}_{q+p})(i\omega_m - E^{\pm}_q)}, \tag{A13}$$

with $E_q^{\pm} = \pm E_q$. In Eq. (A11) the sum runs over all possible combinations of the signs of $E^{\pm}_{q+p}$ and $E^{\pm}_q$. It is enough to calculate only one term of the sum, for example $\mathcal{T}_M^{++}$ and $\mathcal{S}^{++}$, and the others can be obtained by an appropriate choice of signs. Below we skip these signs and recover them in the final expressions. The computation of traces gives

$$\mathcal{T}_M = N_cN_f\frac{P_M m^2 + E_{q+p}E_q - \boldsymbol{q}\cdot(\boldsymbol{q}+\boldsymbol{p})}{E_{q+p}E_q}, \tag{A14}$$

where $P_\sigma = 1$, and $P_\pi = -1$.

The sum over the Matsubara frequencies gives

$$\mathcal{S} = \frac{n^+(E_q) - n^+(E_{q+p})}{E_q - E_{q+p} + i\omega_n}. \tag{A15}$$

Using the results (A14) and (A15) we find for the polarization tensor (A11)

$$\Pi_M(\boldsymbol{p},\omega_n) = -N_cN_f\int\frac{d\boldsymbol{q}}{(2\pi)^3}\left\{\frac{P_M m^2 + E_{q+p}E_q - \boldsymbol{q}\cdot(\boldsymbol{q}+\boldsymbol{p})}{E_{q+p}E_q}\left[\frac{n^+(E_q) - n^+(E_{q+p})}{E_- + i\omega_n} - \frac{n^-(E_q) - n^-(E_{q+p})}{-E_- + i\omega_n}\right] + \frac{P_M m^2 - E_{q+p}E_q - \boldsymbol{q}\cdot(\boldsymbol{q}+\boldsymbol{p})}{E_{q+p}E_q}\left[\frac{n^-(E_q) + n^+(E_{q+p}) - 1}{-E_+ + i\omega_n} - \frac{n^+(E_q) + n^-(E_{q+p}) - 1}{E_+ + i\omega_n}\right]\right\}, \tag{A16}$$

with $E_\pm = E_q \pm E_{q+p}$. Define the short-hand notation $N_M(\boldsymbol{p},\omega_n) = -(\boldsymbol{p}^2 + \omega_n^2) - 2(1 + P_M)m^2$, which gives for the π- and σ-modes, respectively, $N_\pi(\boldsymbol{p},\omega_n) = -(\boldsymbol{p}^2 + \omega_n^2)$ and $N_\sigma(\boldsymbol{p},\omega_n) = N_\pi(\boldsymbol{p},\omega_n) - 4m^2$. Then Eq. (A16) can be written in a compact form

$$\Pi_M(\boldsymbol{p},\omega_n) = 2N_cN_f[2I_1 + N_M(\boldsymbol{p},\omega_n)I_2(\boldsymbol{p},\omega_n)], \tag{A17}$$

where

$$I_2(\boldsymbol{p},\omega_n)=\int\frac{d\boldsymbol{q}}{(2\pi)^3}\frac{1}{4E_qE_{q-p}}\left\{\frac{2E_+}{\omega_n^2+E_+^2}+\frac{(i\omega_n-E_+)[n^-(E_q)+n^+(E_{q-p})]-(i\omega_n+E_+)[n^+(E_q)+n^-(E_{q-p})]}{\omega_n^2+E_+^2}\right.$$
$$\left.+\frac{(i\omega_n+E_-)[n^+(E_q)-n^+(E_{q-p})]-(i\omega_n-E_-)[n^-(E_q)-n^-(E_{q-p})]}{\omega_n^2+E_-^2}\right\},\tag{A18}$$

with redefined $E_\pm=E_q\pm E_{q-p}$.

Now we can write the meson propagator according to Eqs. (A9) and (A17) as

$$D_M^{-1}(\boldsymbol{p},\omega_n)=G^{-1}-2N_cN_f[2I_1+N_M(\boldsymbol{p},\omega_n)I_2(\boldsymbol{p},\omega_n)].\tag{A19}$$

The momentum-independent meson mass is defined as the pole of the propagator in real space-time for $\boldsymbol{p}=0$ ($i\omega_n\to m_M+i\delta$)

$$\mathrm{Re}D_M^{-1}[\boldsymbol{0},-i(m_M+i\delta)]=0,\tag{A20}$$

or,

$$m_\pi^2I_2(\boldsymbol{0},-im_\pi)=\frac{1-4GN_cN_fI_1}{2GN_cN_f},\tag{A21}$$

$$(m_\sigma^2-4m^2)I_2(\boldsymbol{0},-im_\sigma)=\frac{1-4GN_cN_fI_1}{2GN_cN_f},\tag{A22}$$

where we took into account that $\mathrm{Re}I_2[\boldsymbol{0},-i(m_M+i\delta)]=I_2(\boldsymbol{0},-im_M)$ in principal-value prescription. From Eq. (A18) we have for $\boldsymbol{p}=0$ ($E_-=0$, $E_+=2E_q$)

$$I_2(\boldsymbol{0},\omega_n)=\frac{1}{8\pi^2}\int_0^\Lambda q^2dq\frac{1-n^+(E_q)-n^-(E_q)}{E_q(E_q^2+\omega_n^2/4)},\tag{A23}$$

and after analytic continuation $i\omega_n\to\omega+i\delta$ we obtain

$$\mathrm{Re}I_2(\boldsymbol{0},\omega)=I_2(\boldsymbol{0},-i\omega)=\frac{1}{8\pi^2}\int_m^{E_\Lambda}qdE_q\frac{1-n^+(E_q)-n^-(E_q)}{E_q^2-\omega^2/4},\tag{A24}$$

where $E_\Lambda=\sqrt{m^2+\Lambda^2}$. For $m<\omega/2$ the integrand of Eq. (A24) has a single pole, and the integral should be understood in the sense of its principal value. For $\omega>0$ we have

$$\mathrm{Im}I_2(\boldsymbol{0},\omega)=\frac{\sqrt{\omega^2-4m^2}}{16\pi\omega}\frac{\sinh(\beta\omega/2)\theta(\omega-2m)}{\sinh(\beta\omega/2)+\cosh(\beta\mu)}\times\theta(2E_\Lambda-\omega).\tag{A25}$$

As seen from Eq. (A25), the pion propagator obtains an imaginary part when $\omega>2m$, therefore it becomes unstable to the on-shell decay into a quark-antiquark pair.

From Eqs. (A6), (A7), (A21), (A22), and (A24) we obtain the following equation for m_π and m_σ

$$1=\frac{GN_cN_f}{\pi^2}\int_m^{E_\Lambda}qdE(E^2-\alpha_Mm^2)\frac{1-n^+(q)-n^-(q)}{E^2-(m_M/2)^2},\tag{A26}$$

where $\alpha_\pi=0$, $\alpha_\sigma=1$. The solutions provided by Eq. (A26) are displayed in Fig. 4 and are discussed in the main text.

The Mott temperature T_M, defined by the condition $m_\pi=2m$, can be found from the following equation

$$\frac{GN_cN_f}{\pi^2}\int_0^\Lambda dqE[1-n^+(q)-n^-(q)]=1.\tag{A27}$$

Now we evaluate the meson propagator using the standard mass-pole approximation (the imaginary part of the pion self-energy is neglected)

$$D_M(\boldsymbol{p},-i\omega)=\frac{-g_M^2}{\omega^2-\boldsymbol{p}^2-m_M^2+i\varepsilon},\tag{A28}$$

where the quark-meson coupling is defined as the residue of the full meson propagator at vanishing momentum

$$g_M^{-2}=-\frac{d}{d\omega^2}D_M^{-1}[\boldsymbol{0},-i\omega]|_{\omega^2=m_M^2}.\tag{A29}$$

Employing Eqs. (A19) and (A23) we obtain for the π- and σ-modes

$$g_\pi^{-2}=2N_cN_f[I_2(\boldsymbol{0},-im_\pi)+m_\pi^2\frac{d}{d\omega^2}I_2(\boldsymbol{0},-i\omega)|_{\omega^2=m_\pi^2}],\tag{A30}$$

$$g_\sigma^{-2}=2N_cN_f[I_2(\boldsymbol{0},-im_\sigma)+(m_\sigma^2-4m^2)\frac{d}{d\omega^2}I_2(\boldsymbol{0},-i\omega)|_{\omega^2=m_\sigma^2}].\tag{A31}$$

To compute the derivative appearing in Eqs. (A30)–(A31) one can formally replace $d/d\omega^2\to-\frac{1}{4}(d/dE_q^2)$ in Eq. (A24) and integrate by parts to obtain

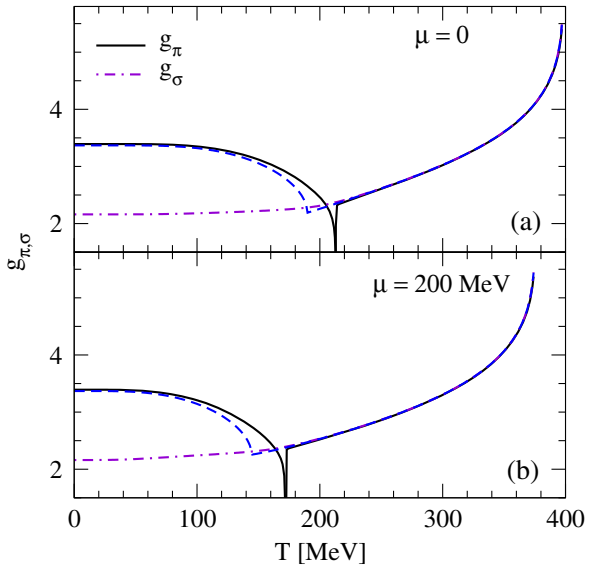

FIG. 16. Dependence of the couplings g_π and g_σ on temperature for zero and nonzero chemical potentials. The chiral limit for the π-meson is shown by short-dashed lines.

$$64\pi^2 \frac{d}{d\omega^2} I_2(\mathbf{0}, -i\omega) = -\frac{\Lambda[1 - n^+(E_\Lambda) - n^-(E_\Lambda)]}{E_\Lambda(E_\Lambda^2 - \omega^2/4)} + \int_m^{E_\Lambda} dE_q \frac{1}{q(E_q^2 - \omega^2/4)} \times \left\{ \frac{m^2}{E_q^2}[1 - n^+(E_q) - n^-(E_q)] + \frac{q^2}{E_q T}[n^+(E_q)(1 - n^+(E_q)) + n^-(E_q)(1 - n^-(E_q))] \right\}. \quad \text{(A32)}$$

Figure 16 shows the temperature dependence of the couplings at zero and nonzero chemical potentials. Note that the jump in the coupling of the π-meson arises at the Mott temperature, i.e., $g_\pi \to 0$ at $T \to T_{\rm M}$, which can be verified from Eq. (A30), where the integral (A32) diverges for $\omega \to 2m$. The two couplings are almost identical above the Mott temperature.

In the chiral limit the overall behavior of the coupling constants remains the same, except for the absence of a discontinuity in the π-meson coupling at the Mott line. Above the Mott temperature the π- and σ-meson coupling constants nearly coincide.

APPENDIX B: MESON-EXCHANGE QUARK SELF-ENERGY

Here we provide some details of the computation of the self-energy (60) and its imaginary part. Analogous calculations for relativistic nucleonic matter were carried out in Ref. [63] and for two-flavor quark matter in Ref. [35].

Substituting the quark and meson propagators into Eq. (60), see Eqs. (A3), (A4), (A28), we find

$$\Sigma^M(\boldsymbol{p}, \omega_n) = g_M^2 \int \frac{d\boldsymbol{q}}{(2\pi)^3 2} \sum_\pm \frac{1}{2E_q^\pm} \times T \sum_m \frac{\Gamma_M(E_q^\pm \gamma_0 - \boldsymbol{\gamma}\cdot\boldsymbol{q} + m)\Gamma_M}{(i\omega_m - E_q^\pm)[(\omega_n - \omega_m)^2 + E_M^2]}, \quad \text{(B1)}$$

where $E_M^2 = (\boldsymbol{p} - \boldsymbol{q})^2 + m_M^2$. For $\Gamma_\sigma = 1$ and $\Gamma_\pi = i\gamma_5\tau_j$ we can write $\Gamma_M(E_q^\pm\gamma_0 - \boldsymbol{\gamma}\cdot\boldsymbol{q} + m)\Gamma_M = E_q^\pm\gamma_0 - \boldsymbol{\gamma}\cdot\boldsymbol{q} + P_M m$, with $P_\sigma = 1$, $P_\pi = -1$, therefore

$$\Sigma^M(\boldsymbol{p}, \omega_n) = P_M m \Sigma_s^M + i\omega_n\gamma_0\Sigma_0^M - \boldsymbol{p}\cdot\boldsymbol{\gamma}\Sigma_v^M, \quad \text{(B2)}$$

where we defined

$$\Sigma_s^M = g_M^2 \int \frac{d\boldsymbol{q}}{(2\pi)^3} \sum_\pm \frac{\mathcal{S}^\pm}{2E_q^\pm}, \quad \text{(B3)}$$

$$\Sigma_0^M = g_M^2 \int \frac{d\boldsymbol{q}}{(2\pi)^3} \frac{1}{2i\omega_n} \sum_\pm \mathcal{S}^\pm, \quad \text{(B4)}$$

$$\Sigma_v^M = g_M^2 \int \frac{d\boldsymbol{q}}{(2\pi)^3} \frac{\boldsymbol{q}\cdot\boldsymbol{p}}{p^2} \sum_\pm \frac{\mathcal{S}^\pm}{2E_q^\pm}, \quad \text{(B5)}$$

and

$$\mathcal{S}^\pm = \frac{1}{2E_M}\left[\frac{n^+(E_q^\pm) + n_B(-E_M)}{E_q^\pm + E_M - i\omega_n} - \frac{n^+(E_q^\pm) + n_B(E_M)}{E_q^\pm - E_M - i\omega_n}\right]. \quad \text{(B6)}$$

Defining $E_\pm = E_q \pm E_M$ and using the properties $n_B(-E) = -1 - n_B(E)$, $n^+(-E) = 1 - n^-(E)$ we obtain

$$\sum_\pm \mathcal{S}^\pm = \frac{1}{2E_M}\left[\frac{E_+\mathscr{L}_3 - 2i\omega_n\mathscr{L}_1}{E_+^2 + \omega_n^2} - \frac{E_-\mathscr{L}_3 + 2i\omega_n\mathscr{L}_2}{E_-^2 + \omega_n^2}\right], \quad \text{(B7)}$$

where $\mathscr{L}_1$, $\mathscr{L}_2$, and $\mathscr{L}_3$ are defined in Eqs. (64). In the same manner we obtain

$$\sum_\pm \frac{\mathcal{S}^\pm}{2E_q^\pm} = \frac{1}{4E_qE_M}\left[\frac{i\omega_n\mathscr{L}_3 - 2E_+\mathscr{L}_1}{E_+^2 + \omega_n^2} - \frac{i\omega_n\mathscr{C}_3 + 2E_-\mathscr{C}_2}{E_-^2 + \omega_n^2}\right]. \quad \text{(B8)}$$

Now using Eqs. (B7) and (B8) in Eqs. (B3)–(B5) we obtain Eqs. (62) and (63) of the main text.

We now turn to the computation of the imaginary parts of Eqs. (62) and (63), which are extracted using the Dirac identity by writing

$$\mathrm{Im}\frac{1}{E^2+\omega_n^2}|_{i\omega_n\to p_0+i\varepsilon} = \pi\mathrm{sgn}(p_0)\delta(E^2-p_0^2) = \frac{\pi}{2p_0}[\delta(E+p_0)+\delta(E-p_0)]. \tag{B9}$$

For on-shell quarks with $p_0=\sqrt{\boldsymbol{p}^2+m^2}$ Eqs. (62) and (63) generate four contributions after analytical continuation and application of the Dirac identity, each of which is proportional to a δ-function

$$\delta(E_M+E_q+p_0)\equiv\delta_1, \quad \delta(E_M+E_q-p_0)\equiv\delta_2, \tag{B10}$$

$$\delta(E_M-E_q+p_0)\equiv\delta_3, \quad \delta(E_M-E_q-p_0)\equiv\delta_4. \tag{B11}$$

For $p_0\geq 0$, the term δ_1 vanishes trivially. As we will show later, the terms δ_2 and δ_3 do not give any contribution as well. For δ_4 we can write

$$\delta_4=\frac{E_M}{pq}\delta(x-x_-), \quad x_-=\frac{m_M^2-2m^2-2E_qp_0}{2pq}, \tag{B12}$$

and for an arbitrary function $f(\boldsymbol{q})$ we then have

$$\int\frac{d\boldsymbol{q}}{(2\pi)^3}f(\boldsymbol{q})\delta_4=\int_{E_{\min}}^{E_{\max}}\frac{dE_q}{(2\pi)^2}\frac{E_qE_M}{p}f(q,x_-), \tag{B13}$$

where the limits of integration are found from the condition $x_-^2\leq 1$

$$\left(\frac{m_M^2-2m^2-2E_qp_0}{2pq}\right)^2\leq 1, \tag{B14}$$

which leads us to Eq. (70) of the main text.

In analogy to Eqs. (B12) and (B13) we have

$$\delta_2+\delta_3=\delta(E_M+E_q-p_0)+\delta(E_M-E_q+p_0) = \frac{E_M}{pq}\delta(x-x_+), \quad x_+=\frac{m_M^2-2m^2+2E_qp_0}{2pq}, \tag{B15}$$

therefore

$$\int\frac{d\boldsymbol{q}}{(2\pi)^3}f(\boldsymbol{q})(\delta_2+\delta_3)=\int_m^\infty\frac{dE_q}{(2\pi)^2}\frac{E_qE_M}{p}f(q,x_+)\theta(1-x_+^2). \tag{B16}$$

The condition $x_+^2\leq 1$ is satisfied for $E_q\in(E'_{\min},E'_{\max})$ with $E'_{\min}=-E_{\max}$, $E'_{\max}=-E_{\min}$, as can be seen from Eq. (70) (note that x_+ is obtained from x_- by the inversion $p_0\to -p_0$). In this case the integration range is empty, and the integral vanishes.

We are now in a position to take the imaginary parts of the self-energies; keeping the only nonvanishing part $\propto \mathrm{Im}[E_-^2+\omega_n^2]^{-1}=\pi(2p_0)^{-1}\delta_4$ we find

$$\mathrm{Im}\Sigma_{s,v}^M=-g_M^2\int\frac{d\boldsymbol{q}}{(2\pi)^3}\mathscr{D}_{s,v}(\boldsymbol{q})\frac{p_0\mathscr{L}_3+2E_-\mathscr{L}_2}{4E_qE_M}\frac{1}{E_-^2+\omega_n^2} = \frac{g_M^2}{16\pi p}\int_{E_{\min}}^{E_{\max}}dE_q\mathscr{D}_{s,v}(q,x_-)[n_B(E_M)+n^-(E_q)], \tag{B17}$$

and

$$\mathrm{Im}\Sigma_0^M=g_M^2\int\frac{d\boldsymbol{q}}{(2\pi)^3}\mathscr{D}_0(q)\frac{2p_0\mathscr{L}_2+E_-\mathscr{L}_3}{4E_qE_M}\frac{1}{E_-^2+\omega_n^2} = \frac{g_M^2}{16\pi p}\int_{E_{\min}}^{E_{\max}}dE_q\mathscr{D}_0(q)[n_B(E_M)+n^-(E_q)]. \tag{B18}$$

Combining Eqs. (B17) and (B18) we finally obtain Eq. (67) of the main text. The imaginary part of the on-shell self-energy of antiquarks ($p_0=-E_p$), given by Eq. (69), is obtained through a similar calculation. To support the discussion of the various contributions to the self-energies (67) and (69) in the main text we show in Fig. 17 the ranges of integration in these equations.

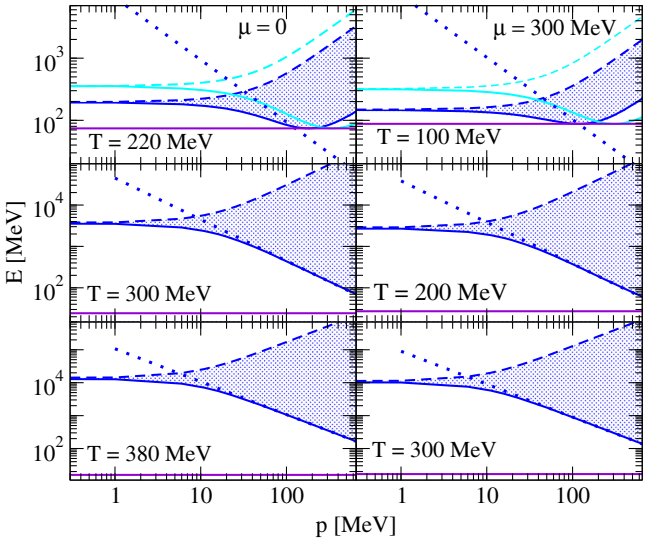

FIG. 17. Dependence of the ranges of integration (shaded area) in the self-energies (67) and (69) on momentum at various values of temperature and chemical potential. The ranges are limited by $E_{\min,\pi}$ (heavy solid line) and $E_{\max,\pi}$ (heavy dashed line) for π-mesons and by $E_{\min,\sigma}$ (light solid line) and $E_{\max,\sigma}$ (light dashed line). The chiral limit Eq. (72) is shown by the dotted lines. The value of the quark mass is shown by the heavy horizontal line.

APPENDIX C: THERMODYNAMIC QUANTITIES

The particle number and entropy densities of quark matter within the $1/N_c$ approximation are given by the formulas

$$n = \frac{N_c N_f}{\pi^2}\int_0^\infty p^2 dp[n^+(E_p) - n^-(E_p)], \tag{C1}$$

$$s = \frac{N_c N_f}{\pi^2}\int_0^\infty p^2 dp[\beta(E_p-\mu)n^+(E_p) + \beta(E_p+\mu)n^-(E_p) - \log(1-n^+(E_p)) - \log(1-n^-(E_p))], \tag{C2}$$

with $n^\pm(E) = [e^{\beta(E\mp\mu)}+1]^{-1}$. The integrals in Eqs. (C1) and (C2) should be calculated without momentum cutoff, but for momenta $p > \Lambda$ the quark energy should be evaluated with its bare mass, i.e., $E_p = \sqrt{p^2+m_0^2}$.

The enthalpy per particle is defined as

$$h = \frac{Ts+\mu n}{n} = \frac{N_c N_f}{\pi^2 n}\int_0^\infty p^2 dp \times \left(E_p + \frac{p^2}{3E_p}\right)[n^+(E_p) + n^-(E_p)]. \tag{C3}$$

Figure 18 shows the quark number density, the enthalpy density, and the enthalpy per particle given by Eqs. (C1) and (C3). In the non-degenerate regime $T \gg \mu$ we distinguish the following limiting cases: (i) $T \gg m$, i.e., high temperatures where chiral symmetry is (approximately) restored; and (ii) $T \ll m$, i.e., the regime where quarks are non-relativistic. In the first case $p \simeq \varepsilon \sim T$, therefore we have the scalings $n \propto \mu T^2$, $nh \propto T^4$, and $h \propto T^2/\mu \to \infty$ at $\mu \to 0$. In the second case the integrands of Eqs. (C1) and (C3) are exponentially suppressed by the distribution function for energies $\varepsilon - m \gtrsim T$, and we find the scalings $n \propto m\mu(mT)^{1/2}e^{-m/T}$, $nh \propto m(mT)^{3/2}e^{-m/T}$, and $h \simeq mT/\mu \gg m$. Thus, the quark number density and the enthalpy density are exponentially suppressed because of the non-vanishing quark condensate at low temperatures. The enthalpy per particle again diverges as the chemical potential tends to zero. In the opposite, strongly degenerate limit $T \ll \mu$ consider the cases: (i) $\mu \gg m$ and (ii) $\Delta \gg T$, where $\Delta \equiv m - \mu$. The first case is realized at high chemical potentials $\mu \gtrsim 350$ MeV, where we have degenerate matter along with (approximate) chiral symmetry restoration. In this case all three quantities depend only on the chemical potential: $n \propto \mu^3$, $nh \propto \mu^4$, and $h \to \mu$. The second case is realized for intermediate values of the chemical potential $\mu \lesssim 300$ MeV, where the constituent quark mass still exceeds the chemical potential. In this case the quark number density and the enthalpy density vanish exponentially when $T \to 0$ according to the scalings $n \propto (mT)^{3/2}e^{-\Delta/T}$, $nh \propto m(mT)^{3/2}e^{-\Delta/T}$, with $\Delta > 0$, and the enthalpy per particle has a finite limit $h \to m$, as seen in Fig. 18.

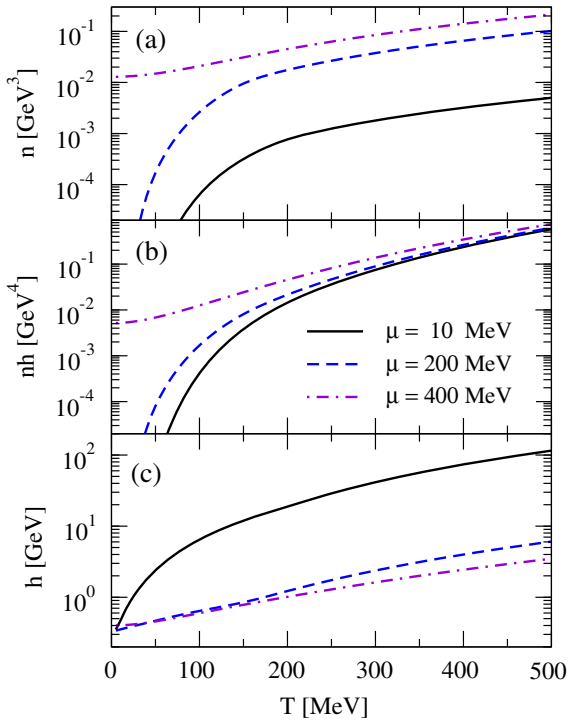

FIG. 18. Dependence of (a) quark number density, (b) enthalpy density, and (c) the enthalpy per particle on the temperature for several values of the chemical potential.

Using Eqs. (C1)–(C2) we can calculate the specific heat of quark matter via the standard formula for the heat capacity per unit volume

$$c_V = T\left(\frac{\partial s}{\partial T}\right)_n = -\beta\left(\frac{\partial s}{\partial \beta}\right)_\mu - \beta\left(\frac{\partial s}{\partial \mu}\right)_\beta \left(\frac{\partial \mu}{\partial \beta}\right)_n. \tag{C4}$$

Using the relations

$$\left(\frac{\partial n^\pm}{\partial \beta}\right)_\mu = -(E_p \mp \mu)n^\pm(1-n^\pm), \tag{C5}$$

$$\left(\frac{\partial n^\pm}{\partial \mu}\right)_\beta = \pm\beta n^\pm(1-n^\pm), \tag{C6}$$

by taking the derivatives of Eq. (C2) we find

$$\left(\frac{\partial s}{\partial \beta}\right)_\mu = -\frac{N_c N_f}{\pi^2 T}\int_0^\infty p^2 dp[(E_p-\mu)^2 n^+(1-n^+) + (E_p+\mu)^2 n^-(1-n^-)], \tag{C7}$$

$$\left(\frac{\partial s}{\partial \mu}\right)_\beta = \frac{N_c N_f}{\pi^2 T^2}\int_0^\infty p^2 dp[(E_p-\mu)n^+(1-n^+) - (E_p+\mu)n^-(1-n^-)], \tag{C8}$$

which implies that Eq. (C4) can be written as

$$c_V = \frac{N_c N_f}{\pi^2 T^2}\int_0^\infty p^2 dp[(E_p-\mu)(E_p-\mu^*)n^+(1-n^+) + (E_p+\mu)(E_p+\mu^*)n^-(1-n^-)], \tag{C9}$$

where we introduced

$$\mu^*(\beta,\mu) = \mu + \beta\left(\frac{\partial\mu}{\partial\beta}\right)_n. \tag{C10}$$

Here we neglected the dependence of the constituent quark mass on the temperature and the chemical potential, as it is of minor importance above the Mott temperature. In order to find $(\partial\mu/\partial\beta)_n$ we take the derivative of Eq. (C1) with respect to β for $n = \text{const}$. As the left-hand side vanishes, we obtain

$$\int_0^\infty p^2 dp[-(E_p-\mu)n^+(1-n^+) + (E_p+\mu)n^-(1-n^-)] + \beta\left(\frac{\partial\mu}{\partial\beta}\right)_n \int_0^\infty p^2 dp[n^+(1-n^+) + n^-(1-n^-)] = 0. \tag{C11}$$

From Eqs. (C10) and (C11) it follows that

$$\mu^*(\beta,-\mu) = -\mu^*(\beta,\mu) \tag{C12}$$

and

$$\int_0^\infty p^2 dp[(E_p-\mu^*)n^+(1-n^+) - (E_p+\mu^*)n^-(1-n^-)] = 0, \tag{C13}$$

therefore Eq. (C9) can be written as

$$c_V = \frac{N_c N_f}{\pi^2 T^2}\int_0^\infty p^2 dp E_p[(E_p-\mu^*)n^+(1-n^+) + (E_p+\mu^*)n^-(1-n^-)], \tag{C14}$$

which is an even function of μ, as expected.

Figure 19 shows the entropy density, the specific heat capacity, and their ratio given by Eqs. (C2) and (C14). In the nondegenerate ultrarelativistic limit $\mu^* \simeq 3\mu \ll T$, s and c_V scale as T^3, therefore their ratio tends to its classical limit $c_V/s \to 3$. In the nondegenerate nonrelativistic limit $(m \gg T \gg \mu)$ we find $\mu^* \propto \mu m/T \ll m$ as well as the scalings $s \propto m^2(mT)^{1/2}e^{-m/T}$ and $c_V \propto m^3(m/T)^{1/2}e^{-m/T}$, which demonstrate the exponential suppression of these quantities by the quark condensate. In this case their ratio $c_V/s \simeq m/T$ diverges as $T \to 0$, as seen from the solid line in panel (c). At very high chemical potentials $\mu \gg T, m$ we find $\mu^* \to \mu$ and the scaling $s \simeq c_V \propto \mu^2 T$, which implies therefore $c_V/s \to 1$. In the degenerate regime when $T \ll \Delta$, the scaling is $s \propto m\Delta(mT)^{1/2}e^{-\Delta/T}$. In order to find the leading term contributing to c_V, we need to keep the first thermal correction in μ^*, which gives $\mu^* \simeq m + 3T/2$. Then the integral (C14) can be estimated as $c_V \propto (mT)^{3/2}e^{-\Delta/T}$, and, therefore, the ratio $c_V/s \propto T/\Delta \to 0$ as $T \to 0$ [see dashed line in panel (c)]. In this limiting case the entropy per particle diverges as $s/n \propto \Delta/T$, and the specific heat per particle tends to the nonrelativistic limit $c_V/n \to 3/2$.

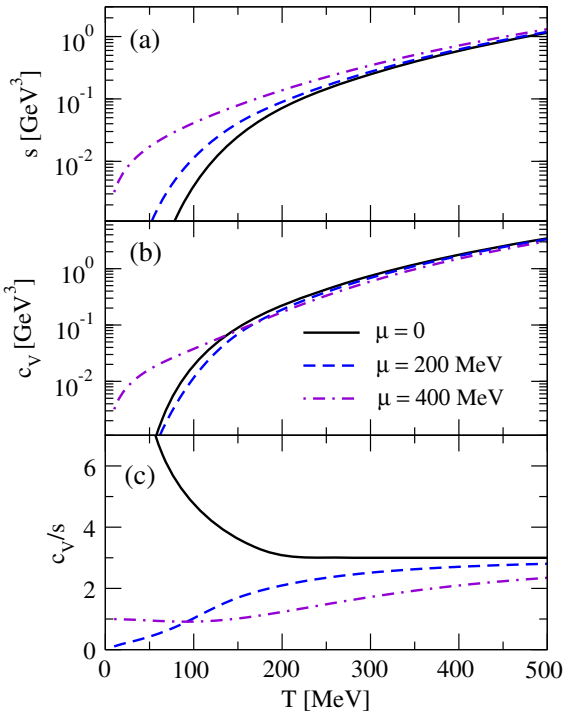

FIG. 19. Dependence of (a) entropy density, (b) specific heat, and (c) their ratio on the temperature for several values of the chemical potential.

[1] M. Gyulassy and L. McLerran, New forms of QCD matter discovered at RHIC, Nucl. Phys. **A750**, 30 (2005).

[2] R. Baier, P. Romatschke, and U. A. Wiedemann, Dissipative hydrodynamics and heavy-ion collisions, Phys. Rev. C **73**, 064903 (2006).

[3] H. Song and U. Heinz, Causal viscous hydrodynamics in $2+1$ dimensions for relativistic heavy-ion collisions, Phys. Rev. C **77**, 064901 (2008).

[4] M. Luzum and P. Romatschke, Conformal relativistic viscous hydrodynamics: Applications to RHIC results at $s_{NN} = 200$ GeV, Phys. Rev. C **78**, 034915 (2008).

[5] M. Luzum and P. Romatschke, Viscous Hydrodynamic Predictions for Nuclear Collisions at the LHC, Phys. Rev. Lett. **103**, 262302 (2009).

[6] H. Song, S. A. Bass, U. Heinz, T. Hirano, and C. Shen, 200 A GeV Au + Au Collisions Serve a Nearly Perfect Quark-Gluon Liquid, Phys. Rev. Lett. **106**, 192301 (2011).

[7] U. Heinz, Towards the little bang standard model, J. Phys. Conf. Ser. **455**, 012044 (2013).

[8] L. P. Csernai, J. I. Kapusta, and L. D. McLerran, Strongly Interacting Low-Viscosity Matter Created in Relativistic Nuclear Collisions, Phys. Rev. Lett. **97**, 152303 (2006).

[9] H. Niemi, G. S. Denicol, P. Huovinen, E. Molnár, and D. H. Rischke, Influence of Shear Viscosity of Quark-Gluon Plasma on Elliptic Flow in Ultrarelativistic Heavy-Ion Collisions, Phys. Rev. Lett. **106**, 212302 (2011).

[10] I. A. Shovkovy and P. J. Ellis, Thermal conductivity of dense quark matter and cooling of stars, Phys. Rev. C **66**, 015802 (2002).

[11] C. Manuel, A. Dobado, and F. J. Llanes-Estrada, Shear viscosity in a CFL quark star, J. High Energy Phys. 09 (2005) 076.

[12] M. G. Alford, H. Nishimura, and A. Sedrakian, Transport coefficients of two-flavor superconducting quark matter, Phys. Rev. C **90**, 055205 (2014).

[13] S. Sarkar and R. Sharma, The shear viscosity of two-flavor crystalline color superconducting quark matter, arXiv: 1701.00010.

[14] B. Friman, C. Höhne, J. Knoll, S. Leupold, J. Randrup, R. Rapp *et al.*, *The CBM Physics Book: Compressed Baryonic Matter in Laboratory Experiments*, Lecture Notes in Physics (Springer, Berlin Heidelberg, 2011).

[15] D. Blaschke, J. Aichelin, E. Bratkovskaya, V. Friese, M. Gazdzicki, J. Randrup, O. Rogachevsky, O. Teryaev, and V. Toneev, Topical issue on exploring strongly interacting matter at high densities—nica white paper, Eur. Phys. J. A **52**, 267 (2016).

[16] Y. Nambu and G. Jona-Lasinio, Dynamical model of elementary particles based on an analogy with superconductivity. I, Phys. Rev. **122**, 345 (1961).

[17] Y. Nambu and G. Jona-Lasinio, Dynamical model of elementary particles based on an analogy with superconductivity. II, Phys. Rev. **124**, 246 (1961).

[18] U. Vogl and W. Weise, The Nambu and Jona-Lasinio model: Its implications for hadrons and nuclei, Prog. Part. Nucl. Phys. **27**, 195 (1991).

[19] S. P. Klevansky, The Nambu-Jona-Lasinio model of quantum chromodynamics, Rev. Mod. Phys. **64**, 649 (1992).

[20] M. Buballa, NJL-model analysis of dense quark matter, Phys. Rep. **407**, 205 (2005).

[21] R. Kubo, Statistical-mechanical theory of irreversible processes. I, J. Phys. Soc. Jpn. **12**, 570 (1957).

[22] D. Zubarev, V. Morozov, and G. Röpke, *Statistical Mechanics of Nonequilibrium Processes* (John Wiley & Sons, New York, 1997).

[23] H. Heiselberg, Viscosities of quark-gluon plasmas, Phys. Rev. D **49**, 4739 (1994).

[24] P. Arnold, G. D. Moore, and L. G. Yaffe, Transport coefficients in high temperature gauge theories (I): leading-log results, J. High Energy Phys. 11 (2000) 001.

[25] P. Arnold, G. D. Moore, and L. G. Yaffe, Transport coefficients in high temperature gauge theories, 2. Beyond leading log, J. High Energy Phys. 05 (2003) 051.

[26] Y. Hidaka and R. D. Pisarski, Suppression of the shear viscosity in a semi, -quark-gluon plasma, Phys. Rev. D **78**, 071501 (2008).

[27] J.-W. Chen, Y.-F. Liu, S. Pu, Y.-K. Song, and Q. Wang, Negative off-diagonal conductivities in a weakly coupled quark-gluon plasma at the leading-log order, Phys. Rev. D **88**, 085039 (2013).

[28] M. Greif, I. Bouras, C. Greiner, and Z. Xu, Electric conductivity of the quark-gluon plasma investigated using a perturbative QCD based parton cascade, Phys. Rev. D **90**, 094014 (2014).

[29] K. Hattori, S. Li, D. Satow, and H.-U. Yee, Longitudinal conductivity in strong magnetic field in perturbative QCD: Complete leading order, Phys. Rev. D **95**, 076008 (2017).

[30] K. Hattori and D. Satow, Electrical conductivity of quark-gluon plasma in strong magnetic fields, Phys. Rev. D **94**, 114032 (2016).

[31] H. Defu, Shear viscosity of hot QCD from transport theory and thermal field theory in real time formalism, hep-ph/0501284.

[32] M. Iwasaki, H. Ohnishi, and T. Fukutome, Shear viscosity of the quark matter, J. Phys. G Nucl. Phys. **35**, 035003 (2008).

[33] W. M. Alberico, S. Chiacchiera, H. Hansen, A. Molinari, and M. Nardi, Shear viscosity and entropy of quark matter, Eur. Phys. J. A **38**, 97 (2008).

[34] R. Lang and W. Weise, Shear viscosity from Kubo formalism: NJL model study, Eur. Phys. J. A **50**, 63 (2014).

[35] R. Lang, N. Kaiser, and W. Weise, Shear viscosities from Kubo formalism in a large-N_c Nambu-Jona-Lasinio model, Eur. Phys. J. A **51**, 127 (2015).

[36] R. Lang, Doctoral thesis, Technische Universität München, 2015.

[37] S. Ghosh, T. C. Peixoto, V. Roy, F. E. Serna, and G. Krein, Shear and bulk viscosities of quark matter from quark-meson fluctuations in the Nambu-Jona-Lasinio model, Phys. Rev. C **93**, 045205 (2016).

[38] S.-x. Qin and D. H. Rischke, Charmonium spectral functions and transport properties of quark-gluon plasma, Phys. Lett. B **734**, 157 (2014).

[39] Z. Xu and C. Greiner, Shear Viscosity in a Gluon Gas, Phys. Rev. Lett. **100**, 172301 (2008).

[40] R. Marty, E. Bratkovskaya, W. Cassing, J. Aichelin, and H. Berrehrah, Transport coefficients from the Nambu-Jona-Lasinio model for $SU(3)_f$, Phys. Rev. C **88**, 045204 (2013).

[41] A. Puglisi, S. Plumari, and V. Greco, Electric conductivity from the solution of the relativistic Boltzmann equation, Phys. Rev. D **90**, 114009 (2014).

[42] S. Plumari, A. Puglisi, F. Scardina, and V. Greco, Shear viscosity of a strongly interacting system: Green-Kubo correlator versus Chapman-Enskog and relaxation-time approximations, Phys. Rev. C **86**, 054902 (2012).
[43] P. Danielewicz and M. Gyulassy, Dissipative phenomena in quark-gluon plasmas, Phys. Rev. D **31**, 53 (1985).
[44] A. S. Khvorostukhin, V. D. Toneev, and D. N. Voskresensky, Viscosity coefficients for hadron and quark-gluon phases, Nucl. Phys. **A845**, 106 (2010).
[45] K. Heckmann, M. Buballa, and J. Wambach, Chiral restoration effects on the shear viscosity of a pion gas, Eur. Phys. J. A **48**, 142 (2012).
[46] S. Ghosh, A. Lahiri, S. Majumder, R. Ray, and S. K. Ghosh, Shear viscosity due to Landau damping from the quark-pion interaction, Phys. Rev. C **88**, 068201 (2013).
[47] H. B. Meyer, Calculation of the shear viscosity in SU(3) gluodynamics, Phys. Rev. D **76**, 101701 (2007).
[48] H. B. Meyer, Transport properties of the quark-gluon plasma from lattice QCD, Nucl. Phys. **A830**, 641 (2009).
[49] G. Aarts, C. Allton, J. Foley, S. Hands, and S. Kim, Spectral Functions at Small Energies and the Electrical Conductivity in Hot Quenched Lattice QCD, Phys. Rev. Lett. **99**, 022002 (2007).
[50] A. Amato, G. Aarts, C. Allton, P. Giudice, S. Hands, and J.-I. Skullerud, Electrical Conductivity of the Quark-Gluon Plasma Across the Deconfinement Transition, Phys. Rev. Lett. **111**, 172001 (2013).
[51] G. Aarts, C. Allton, A. Amato, P. Giudice, S. Hands, and J.-I. Skullerud, Electrical conductivity and charge diffusion in thermal QCD from the lattice, J. High Energy Phys. 02 (2015) 186.
[52] N. Astrakhantsev, V. Braguta, and A. Kotov, Temperature dependence of shear viscosity of $SU(3)$–gluodynamics within lattice simulation, J. High Energy Phys. 04 (2017) 101.
[53] P. K. Kovtun, D. T. Son, and A. O. Starinets, Viscosity in Strongly Interacting Quantum Field Theories from Black Hole Physics, Phys. Rev. Lett. **94**, 111601 (2005).
[54] S. S. Gubser, A. Nellore, S. S. Pufu, and F. D. Rocha, Thermodynamics and Bulk Viscosity of Approximate Black Hole Duals to Finite Temperature Quantum Chromodynamics, Phys. Rev. Lett. **101**, 131601 (2008).
[55] R. Rougemont, J. Noronha, and J. Noronha-Hostler, Suppression of Baryon Diffusion and Transport in a Baryon Rich Strongly Coupled Quark-Gluon Plasma, Phys. Rev. Lett. **115**, 202301 (2015).
[56] S. I. Finazzo and J. Noronha, Holographic calculation of the electric conductivity of the strongly coupled quark-gluon plasma near the deconfinement transition, Phys. Rev. D **89**, 106008 (2014).
[57] D. Li, S. He, and M. Huang, Temperature dependent transport coefficients in a dynamical holographic QCD model, J. High Energy Phys. 06 (2015) 46.
[58] S. Ivo Finazzo and R. Rougemont, Thermal photon and dilepton production and electric charge transport in a baryon rich strongly coupled QGP from holography, Phys. Rev. D **93**, 034017 (2016).
[59] E. Quack and S. P. Klevansky, Effective $1/N_c$ expansion in the Nambu-Jona-Lasinio model, Phys. Rev. C **49**, 3283 (1994).
[60] A. Hosoya, M.-a. Sakagami, and M. Takao, Non-equilibrium thermodynamics in field theory: Transport coefficients, Ann. Phys. (N.Y.) **154**, 229 (1984).
[61] X.-G. Huang, A. Sedrakian, and D. H. Rischke, Kubo formulas for relativistic fluids in strong magnetic fields, Ann. Phys. (Berlin) **326**, 3075 (2011).
[62] N. Christiansen, M. Haas, J. M. Pawlowski, and N. Strodthoff, Transport Coefficients in Yang-Mills Theory and QCD, Phys. Rev. Lett. **115**, 112002 (2015).
[63] G. Colucci, A. Sedrakian, and D. H. Rischke, Leading-order nucleon self-energy in relativistic chiral effective field theory, Phys. Rev. C **88**, 015209 (2013).